Analysis of Bat Biosonar Beampatterns: Biodiversity & Dynamics

Philip Caspers

Dissertation submitted to the Faculty of the

Virginia Polytechnic Institute and State University

in partial fulfillment of the requirements for the degree of

Doctor of Philosophy

in

Mechanical Engineering

Rolf Müller, Chair

Alexander Leonessa

Nicole Abaid

Javid Bayandor

Hongxiao Zhu

December 5, 2016

Blacksburg, Virginia

Keywords: Sonar, Bats, Biomimetic, Beampatterns, Robotics

Analysis of Bat Biosonar Beampatterns: Biodiversity & Dynamics

Philip Caspers

ABSTRACT (ACADEMIC)

Across species, bats exhibit wildly disparate differences in their noseleaf and pinna shapes. Within Rhinolophid and Hipposiderid families, bats actively deform their pinnae and noseleaf during biosonar operation. Both the pinnae and noseleaf act as acoustic baffles which interact with the outgoing and incoming sound; thus, they form an important interface between the bat and its environment. Beampatterns describe this interface as joint time-frequency transfer functions which vary across spatial direction. This dissertation considers bat biosonar shape diversity and shape dynamics manifest as beampatterns. In the first part, the seemingly disparate set of functional properties resulting from diverse pinna and noseleaf shape adaptations are considered. The question posed in this part is as follows: (i) what are the common properties between species beampatterns? and (ii) how are beampatterns aligned to a common direction for meaningful analysis? Hence, a quantitative interspecific analysis of the beampattern biodiversity was taken wherein: (i) 267 different pinnae and noseleaf beampatterns were rotationally aligned to a common direction and (ii) decomposed using principal component analysis, PCA. The first three principal components termed eigenbeams affect beamwidth around the single lobe, symmetric mean beampattern. Dynamic shape adaptations to the pinna and noseleaf of the greater horseshoe bat (*Rhinolophus ferrumequinum*) are also considered. However, the underlying dynamic sensing principles in

use are not clear. Hence, this work developed a biomimetic substrate to explore the emission and reception sonar dynamics of the horseshoe bat. The question posed in this part was as follows: which local feature combinations on either the noseleaf or pinna generate peak dynamic change to the outgoing or incoming sonar information? Flexible noseleaf and pinnae baffles with different combinations of local shape features were developed. These baffles were then mounted to platforms to biomimetically actuate the noseleaf and pinnae during pulse emission and reception. Motions of the baffle surfaces were synchronized to the incoming and outgoing sonar waveform, and the time-frequency properties of the emission and reception baffles were characterized across spatial direction. Different feature combinations of the noseleaf and pinnae local shape features were then ranked for overall dynamic effect.

GRANT INFORMATION

This work was supported by grants from the National Science Foundation (NSF), Army Research Office, and Naval Engineering Education Consortium (NEEC). Additional support was provided by the NSF East Asia and Pacific (EAPSI) Fellowship and the Naval Research Enterprise Intern Program (NREIP).

Analysis of Bat Biosonar Beampatterns: Biodiversity & Dynamics

Philip Caspers

ABSTRACT (PUBLIC)

Certain bats emit echolocation sounds through complex shapes surrounding the nasal sound emission site - called noseleaves. Subsequent echo information is then received through structurally complex pinna on either side of the bat's head. Since the noseleaf and pinnae form the interface between the bat and it's surrounding environment, the noseleaf and pinnae play an important role in the bat's biosonar operation. Beampatterns describe the acoustic properties of the noseleaf and pinna in the biosonar as gain which varies with direction, frequency, and time. In this work, two types of noseleaf and pinnae shape adaptations represented as beampatterns are considered. First, the diversity in noseleaf and pinna beampatterns resulting from biodiversity in noseleaf and pinna shapes is analyzed. This was accomplished by decomposing 267 beampatterns from 98 different species of bats into common building blocks and comparing the effect each building block had on the average bat biosonar beampattern.

In the second part, the dynamic shape adaptations Rhinolophid and Hipposiderid families of bats make to their noseleaf and pinna during biosonar operation are considered. However, the underlying sensing principles dynamic manipulation of the noseleaf and pinna play in biosonar operation are not clear. Hence, this work developed a biomimetic robot sonar to explore the emission and reception dynamics of the horseshoe bat. The question posed in

this part was as follows: which local features on the noseleaf and pinna acoustically interact when combined together to generate peak dynamic change to the outgoing or incoming sonar information? Flexible noseleaf and pinna baffles with different combinations of local shape features were developed. These baffles were then mounted to platforms to biomimetically actuate the noseleaf and pinna during pulse emission and reception. Motions of the baffle surfaces were synchronized to the incoming and outgoing sonar waveform, and the time-frequency properties of the emission and reception baffles were characterized across spatial direction. Different feature combinations of the noseleaf and pinna local shape features were then ranked for overall dynamic effect.

Acknowledgments

I would like to especially thank Dr. Rolf Müller for having provided me this opportunity and taught me so much. Without his financial support and brilliant insights, this work would not have been possible. I would also like to thank my longtime friend, Dr. Alexander Leonessa, for encouragement to continue through to a doctorate degree, his challenging classes which helped me to grow academically, and for the opportunity to roam China together. I am grateful to Dr. Javid Bayandor for his outstanding career advice and his continued mentorship since the time I was an undergraduate in his vibrations class. Finally, I would like to thank Dr. Nicole Abaid and Dr. Hongxiao Zhu for their technical assistance in my work and engaging conversation. My heartfelt thanks goes to the team of undergraduates working in the lab who helped make this work possible with their outstanding work including Allison Yu, Evan Sachdeva, Brandon Nguyen, Andrew Farley, Chris Watford, Thomas Salzman, and Alex Clark. My lab colleagues deserve mention for their invaluable discussions and the moments we shared. Finally, I would like to thank my parents, Col. Jeff Caspers (USMC Ret.) and Anita Caspers for their loving counsel and support.

Contents

List of Figures

List of Tables

Chapter 1

Introduction

1.1 Model Biological System

Active sonar operates using a basic physical principle: sound is emitted into the environment to infer information. Sonar is not only used in engineering applications but also found in nature. Bats, cetaceans, and some birds employ sonar as a strategy to perceive their environment. However, bats are one of the most prolific users of sonar. With active flight and echolocation, bats are highly successful from an evolutionary standpoint. Approximately 1,200 species of bats are distributed across the globe [67]. Bat inhabit diverse environments including deserts, rainforests, and open savannas. Within these environments, bats feed from a wide selection of food sources including arthropods, fish, nectar, and blood [55, 54, 1].

Of the 1,200 bats distributed across the globe, approximately 1,000 echolocate [49]. Hence,

through adaptive radiation, behavioural, physiological, and morphological adaptations can be observed [24]. These adaptations are understood at different levels. For example, it has long been known that bats adapt their sonar calls. Across species, bats emit sounds orally or through their nasal passages [1, 45]. Additionally, bats modulate the harmonic content, duration, amplitude, and timing of their calls - across species and during biosonar operation. For instance, insect eating bats foraging close to vegetation shorten the duration and harmonic content of their orally emitted frequency modulated (FM) calls [53, 42, 56]. Other insect eating species hunting very close to vegetation nasally emit long duration, constant frequency (CF) calls.

The principle behind these two active call strategies is generally well understood. Both strategies help the animal to detect prey. In the latter case, decreasing the FM call duration while flying to background reflecting vegetation allows the animal to detect insects flying close to the vegetation since it allows time for the loud call to subside before the low amplitude insect echo returns [53]. In the former, CF emitting bats detect insects and separate background reflecting clutter using Doppler shifts in the echo made by wingbeat interaction with the CF pulse [28]. However, from our understanding of human hearing (a similar mammalian auditory system), broad band sounds are localized in direction better than narrow band sounds [5]. Similarly, pulse localization in range for radar systems improves by emitting broadband chirps [58]. Nevertheless, bats using either strategy appear indifferent given both navigate successfully in their environments by localizing their self emitted sounds.

Baffle shapes at the biosonar emission and reception apertures form the interface between

the animal and the environment. Bats use intricate pinnae shapes surrounding the ear canal to receive auditory information, Figure 1.1. Nasal emitting bats also feature intricate shapes surrounding the sound emission site, Figure 1.1. These baffles interact with the outgoing and incoming sounds acoustically [11, 12]. Hence, these structures form a critical stage in the bat biosonar system wherein information like direction is encoded.

Significant biological complexity has been invested in morphological adaptations to these baffle shapes. Furthermore, these adaptations appear to happen along slow and fast time scales. Across species, echolocating bats feature radically different noseleaf and pinnae shapes, Figure 1.1. These shape adaptations are hypothesized to be a product of bats settling into new ecological niches over long periods of time [24]. Hence, shape adaptations might be hypothesized to be adaptations to a bat's particular sensor ecology. Indeed, the hallmark of bat biosonar appears to be a customization of its sonar system for a particular sensor ecology [38]. Hence, looking at the shape customizations bats make to their sonar for sensing purposes might prove a fruitful avenue for bioinspiration. This is the focus of the first part of this work.

Additional, fast morphological shape changes are found in Rhinolophid and Hipposiderid families of bats during biosonar operation. This represents a radical innovation to the static noseleaf and pinnae shapes commonly observed in bats. Motion occurs both in the noseleaf and pinnae. However, the mechanism wherein motion imparts beneficial sensing properties to the animals biosonar system is less well understood. Motion of the noseleaf has been documented to move in two parts of the noseleaf in time with the pulse emission [10, 19]. In

flight, the sensor beamwidth has been shown to change when capturing an insect prey. This is speculated to be due to noseleaf motion [32]. Reported pinnae motions have included rotating and deforming motions alternating between the left and right pinnae [17, 16, 48, 47]. Early anatomical exploration of the pinnae indicate the pinnae surface contains 20 interconnected muscles [51]. Furthermore, pinnae motion is speculated to influence the animals ability to avoid objects vertically since horseshoe bats in flight with disabled pinnae localized obstacles less well vertically [35]. Although substantial evidence points towards the motion of the pinnae and noseleaf playing a role in biosonar operation, the underlying dynamic principles in biosonar sensing are less well understood. This is the focus of the second part of this work.

For both dynamic and static shapes, beampatterns describe the functional properties shape imparts to a bat biosonar system, Figure 1.2. Waves interact with structural features on the noseleaf and pinnae through diffraction. This process happens at different wavelengths which result in strong frequency dependent diffraction properties which vary with direction of the incident or outgoing wave. Salient features in the beampattern are used describe its role in biosonar sensing tasks. Notches in the beampattern frequency response function in different spatial directions are used to explain source localization cues in the big brown bat [3]. In certain cases, shape features correlate with localization information. For example, removal of a flap feature at the base of a brown long-eared bat pinnae (*Plecotus auritus*) is correlated to decrease localization acuity [39]. Study of beampatterns and the relevant biosonar sensing information it contains is largely limited to an individual species level with a few exceptions

[30, 36, 43]. However, sonar is a shared sensing principle across many shape species noseleaf and pinnae shape adaptations, yet the underlying principles bats might use to adapt their biosonar systems through shape morphology is yet unknown. Moreover, noseleaf and pinnae motion adds an additional time dimension to the properties of the animal's biosonar. While evidence suggests plays a role in biosonar operation, the underlying principles are not well understood. This work seeks to take a step forward in each of these areas.

Figure 1.1: Examples of noseleaf and pinnae diversity in echolocating bats: (a) Stoliczka's trident bat (*Aselliscus stoliczkanus*), (b) serotine bat (*Eptesicus serotinus*), (c) pipstrelle bat (*Pipistrellus sp.*), (d) great roundleaf bat (*Hipposideros armiger*), (e) mouse eared bat (*Myotis sp.*), (f) greater horseshoe bat (*Rhinolophus ferrumequinum*)

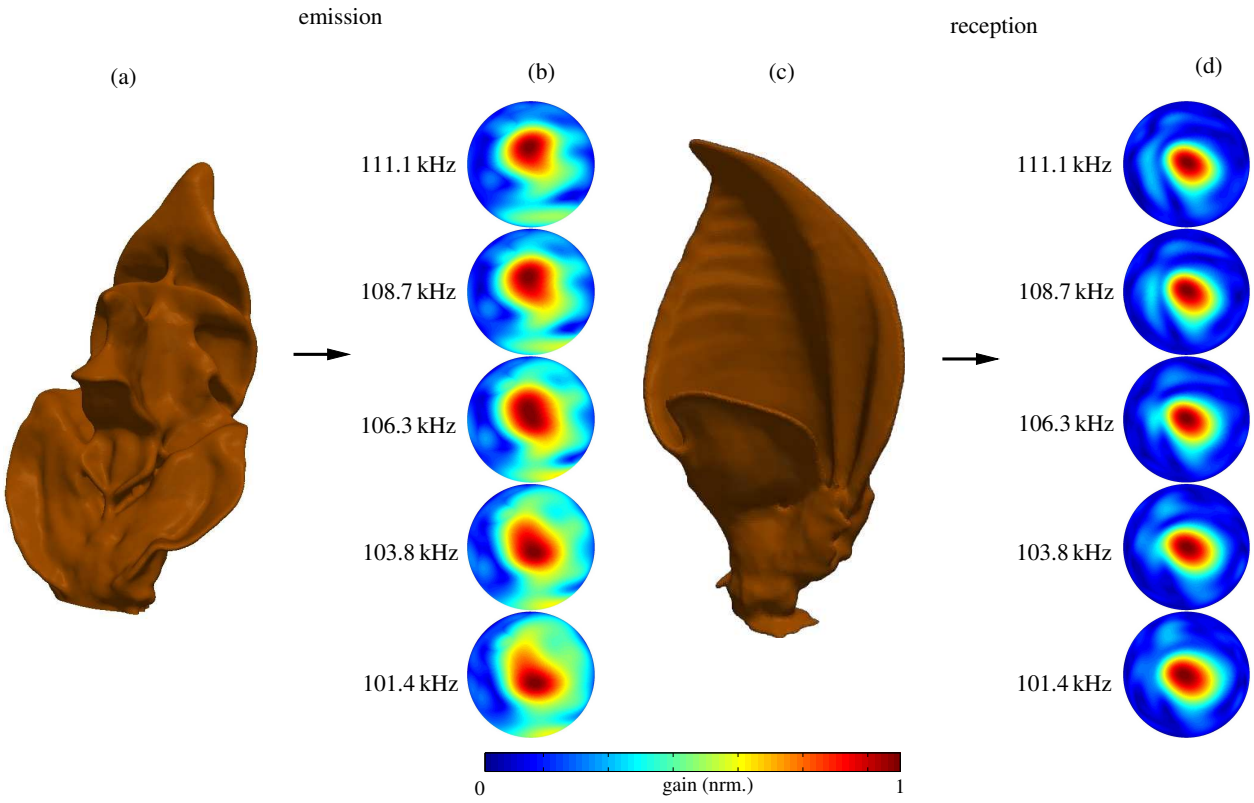

Figure 1.2: Beampatterns describe the spatial and frequency dependent transfer function properties between sound and the noseleaf and pinnae morphology (a) least horseshoe bat (*Rhinolophus pusillus*) noseleaf geometry, (b) emission gain as a function of spatial direction and frequency, (c) pinnae geometry of least horseshoe bat, (d) reception gain directivity pattern

1.2 Motivation for Bioinspiration

Bat biosonar is notable for its elaborate static and dynamic shape adaptations. Both types of shape adaptations represent a radical departure from currently engineered sonar systems.

Technical sonar systems typically consist of multiple sensor elements arranged across an array [62]. For example, towed sonar arrays are made from hundreds of hydrophones distributed along a flexible line thousands of feet long [29]. Combining information from each sensor element across the aperture allows information about the impinging wavefront to be inferred [29, 62]. To improve array performance, the array aperture size is increased. However, this comes at a cost since the complexity associated with increased number of elements and mechanical size proportionally increases [14].

In contrast, bats offer a more parsimonious approach. Bats use relatively few elements in a small mechanical form factor. However, what bats lack in number of elements and aperture size, they make up for in complexity of their noseleaf and pinnae shapes. As an example, bumblebee bats which weigh about 2 g have fully functional sonar systems with highly adapted pinnae and nose shapes [60].

Comparison between technical and bat biosonar performance is mismatched since the requirements and constrains of each system differ. However, the ability for bats to operate under difficult sensing environments is noteworthy given the performance of technical sonar systems in similar environments. Bats hunting near vegetation successfully navigate in cluttered unstructured environments and identify prey hidden within the clutter. In comparison, naval sonars perform poorly in similar littoral environments as evidenced by the fact current technology still relies on marine mammals like dolphins and sea lions to locate buried and difficult to find objects underwater [50]. Hence, biological sonar contains hitherto unexplored principles and thus bioinspiration from bats has potential to impact current sonar

technology. This is also true of other general wave sensing techniques of which sonar is one example. Radars, communication systems, non-destructive testing techniques, and biomedical ultrasound are examples of similar active wave sensing techniques. Hence, bioinspiration from bats has potential to have lasting impact on current technology today.

1.3 Approach

In this work, morphological adaptations at slow and fast levels expressed as static and time-variant beampatterns are addressed in two parts. In the first part, the overall goal is to understand the biodiversity in beampattern construction across many species of bats. It is hypothesized that individual bat beampatterns are adapted from common principles. Studies to date generally consider individual species or handfuls of them. Moreover, these studies that compare beampattern properties across species do so in compressed way as to loose insight about the actual differences [43, 36]. This work seeks to address this issue by considering common properties across beampatterns in high fidelity. This approach comes with a caveat, however. Comparing properties across different species' beampatterns implies there is a common way to compare to beampatterns. This is not the case in reality because beampatterns are a function of pinnae and noseleaf morphology and these shapes are oriented differently by species. Nevertheless, comparison to a common direction is necessary for meaningful analysis. Hence, two questions in the first part are considered: (i) what does it mean to compare different beampatterns across species and (ii) what are the common

biosonar beampattern properties across species? In this part, the beampattern properties of the bat biosonar are considered static in time.

In the second part, a biomimetic method to explore time variant beampatterns in horseshoe bats is developed. *en-vivo* studies of baffle motions are difficult for two reasons: (i) feasibility and (ii) repeatability. First, it is not possible force a live animal to repeat a baffle motion over the thousands of iterations it is necessary to measure the baffles spatial and time-frequency properties. Second, if the motion does occur unsolicited, there is no guarantee the animal will repeat the motion again. Hence a biomimetic robotic approach is taken to studying the time-dynamics of the horseshoe bat. The goal of this part is to develop the pieces necessary to make a time-dynamic sonarhead capable of mimicking the horseshoe bat and demonstrating it has time variant properties. Since local shape features of both the pinnae and noseleaf influence the biosonar properties, this work asks the question how local shape features interact in the pinnae and noseleaf individually and together as design features to make time-dynamic beampatterns.

1.4 Chapter Outline

Chapter 1 - introduction

Chapter 2 - develops a method to align bat biosonar beampatterns and breaks down the common features of the interspecific diversity in beampatterns

Chapter 3 - develops and characterizes a robotic model of the shape motions in horseshoe

bats

Chapter 4 - conclusions

Chapter 2

Bat biosonar biodiversity analysis

2.1 Executive Summary

A quantitative analysis of the interspecific variability in bat biosonar beampatterns has been carried out on 267 numerical predictions of emission and reception beampatterns from 98 different species. Since these beampatterns did not share a common orientation, an alignment was necessary to analyze the variability in the shape of the patterns. To achieve this, beampatterns were aligned using a pairwise optimization framework based on a rotation-dependent cost function. The sum of the p-norms between beam-gain functions across frequency served as a figure of merit. For a representative subset of the data, it was found that all pairwise beampattern alignments resulted in a unique global minimum. This minimum was found

to be contained in a subset of all possible beampattern rotations that could be predicted by the overall beam orientation. Following alignment, the beampatterns were decomposed into principal components. The average beampattern consisted of a symmetric, positionally static single lobe that narrows and became progressively asymmetric with increasing frequency. The first three "eigenbeams" controlled the beamwidth of the beampattern across frequency while higher rank eigenbeams account for symmetry and lobe motion. Reception and emission beampatterns could be distinguished (85 % correct classification) based on the first 14 eigenbeams.

2.2 Introduction

Through the process of adaptive radiation bats have been able to settle in a diverse range of environments from forests to open savannas and exploit an equally diverse range of food sources from insectivores to highly specialized fish, blood, and nectar feeders [24, 54, 59, 1]. It may be hypothesized that the diverse sensory ecology of bat biosonar has been a major enabling factor for this diversification. Within the biosonar system, beampatterns are acoustic functions that represent a complete characterization of the interface between the bat and the outgoing and incoming sounds in the physical domain [43, 69, 3, 39]. The diversity in these functions are not only conspicuous results of the diverse sensor ecology in bats but also represent a radical departure from beampatterns of technical wave-based systems [38].Technical systems typically consist of simple narrow beamwidth beampatterns; however,

bat beampatterns often feature wide beamwidths, non-stationary directional behavior, and the splitting up of single lobes into multiple side-lobes across frequency [38]. If bat biosonar beampatterns are seen as adaptations of general design principles, then understanding this diversity is a step towards distilling general design principles from nature with potential application to wave-based sensing systems.

Previously, beampattern variability has been investigated using a truncated spherical harmonic spectrum representation [36]. This work found that a short vector of spherical harmonic coefficients was sufficient to distinguish beampatterns from different classes (e.g. families and emission-reception beampatterns). However, due to the lossy nature of this beampattern representation, it was not possible to understand the trends in the variability of the beampatterns in terms of beampattern shape, other than beamwidth which was found to be an important factor in beampattern diversity in this work.

The work presented here has taken a step further in understanding the beampattern biodiversity using non-parametric analysis while preserving beampattern geometry. This is accomplished by use of principal component analysis (PCA). PCA describes a dataset by a rotation of the original data vector space along axes describing the greatest variance [23]. Hence, the first eigenaxis will point along the direction of greatest variance and the second axis will point along the orthogonal direction of second greatest variance, and so forth.

PCA has already been used to decompose the morphology of the bat outer ears (pinnae)[30]. It was found that the average of all pinna shapes as well as the first few resultant eigenvectors ("eigenears") had simple geometries that could intuitively understood and used to describe

the major variations in pinna shape about the average. The goal of the current work has been to determine if a similar analysis can be carried out on the biosonar beampatterns of bats. If meaningful principal components can be obtained for the beampatterns as was possible for the pinna shapes, these components could be expressed in the original beampattern space as "eigenbeams" to visualize the directions of the main variability in the beampatterns. In addition, the beampattern of an individual species can then be described as a weighted sum of eigenbeams in classified based on where it is located in the eigenbeam space, e.g., by which eigenbeams carry the most weight.

However, meaningful analysis of trends in beampattern shape using eigenbeams depends on the original beampatterns being aligned to a common direction, [44, 8]. Achieving this is complicated by the interspecific variability in how the noseleaves and pinnae that are responsible for the creation of the beampatterns are physically oriented with respect to the head. Since the data available for the work presented here consists of beampattern predictions obtained for isolated noseleaf and pinna shapes, this information cannot be recovered. Furthermore, certain bats dynamically alter the shape of their ears or orient their heads to best suit their specific sensing scenario, thereby changing the principle orientation of the beampattern [54, 56]. In these cases, using a "natural alignment" between beampatterns is not only prohibited by lack of information, but a single static natural alignment between beampatterns does not exist.

To address this issue, the research presented here has developed an optimization approach to beampattern alignment based on beampattern shape. This alignment has provided the

opportunity to conduct a PCA-based analysis of the variability in the beampattern shapes, which can then be evaluated in terms of its ability to represent this variability in terms of shape patterns that can be readily understood.

2.3 Methods

2.3.1 Dataset

The analysis of the diversity in the beampatterns was carried out over 267 different beampattern estimates derived from specimens representing 98 different species. The beampattern estimates were made numerically based on digital models of pinnae and noseleaf geometry obtained from the specimens *post mortem* [37]. The beampattern estimates analysed here represented nine different bat families: Rhinolophidae (81 beampatterns), Vespertilionidae (67), Hipposideridae (47), Phyllostomidae (34), Nycteridae (15), Pteropodidae (10), Molossidae (6), Emballonuridae (5), and Megadermatidae (2). Hence, the four families with the largest sample size accounted for 85 % of all the beampatterns in the dataset. The estimates in the data set were for emission (142 samples, obtained for noseleaf shapes) as well as reception beampatterns (125 samples, obtained for pinnae shapes).

The beampattern estimates were stored as linear gain values that were sorted by direction (encoded as azimuth and elevation) and frequency. Each beampattern was sampled linearly at 10 frequencies across the emission frequency range of the respective species as documented

in the literature. For each of these frequencies, direction was sampled using an equal area, isolatitude pixel grid with a total of 3072 points across the unit sphere[15].

2.3.2 Alignment optimization problem

The alignment problem for the beampatterns was cast as an optimization problem where a metric for the difference between two beampattern functions was minimized through rotation of one beampattern with respect to the other. The beampatterns were then aligned by the rotation that minimized the difference metric. To define this alignment framework two things are required: i) a rotation parametrization of the search domain and ii) a penalty or cost function to quantify difference between the beampattern functions.

The behaviour of the cost functions of the optimization problem, i.e., the values of difference metric as a function of rotation, was characterized using visualizations of the sampled cost function for a set of example beampatterns over the entire rotation space. Specifying a rotation in three dimensions requires three parameters for which several choices are available[57, 9]. For the purpose of visualizing the cost functions behaviour, an axis-angle parametrization of the rotation space was chosen because the coordinates of points in this space can be readily interpreted by the observer. In the axis-angle parametrization, the rotation is described by the orientation of the axis about which the rotation is performed (given by an azimuth and an elevation angle) and the angle of the rotation about this axis. A spherical coordinate system was used to visualize these three parameters: the azimuth

and elevation coordinates where taken to represent the orientation of the rotation axis and the radius represented the right-hand rotation magnitude about the axis [9]. For the implementation of the rotation operation, each point in this spherical coordinate system was related to its equivalent quaternion-based rotation matrix [65]. In order to obtain a sampled version of the cost function, the rotation space was sampled on a uniform grid using method prescribed by Yershova [71].

To be useful for rotational alignment of the beampatterns, the cost function should have a unique global minimum. Moreover, to perform the alignment fast and reliably for large numbers of beampatterns, it is also desirable that the global minimum is well distinguished from local minima by its depth and that it can be readily found, e.g., by following a large-scale gradient of the cost function or with the help of prior information.

$$\sum_{f=0}^{N_f} w_f \left(\sum_{i=0}^{N_s} |g_{1,f}[i] - g_{2,f}[i]|^p \right)^{1/p} \tag{2.1}$$

A p-norm was used as a distance metric for the beampattern functions [21]. In Eq. 2.1, $g_{1,f}$ and $g_{2,f}$ are the two beampatterns at the f-th frequency for which the distance is computed, f is the index to the N_f frequencies, w_f is a weighting applied to each frequency, and i is the index to the N_s sampling points. The weighting applied was inversely proportional to the integral of the gain over all spherical directions, S, at each frequency, Eq. 2.2.

$$w_f = \left(\int_S g_{1,f}(s)\ ds \right)^{-1} \tag{2.2}$$

The exponent p was adjusted to improve the separation of the global minimum from local minimum over a set of test cases.

2.3.3 Exploration of cost function properties

A dataset of 10 example beampatterns was used to characterize the cost functions to be used for the beampattern alignment. In this example dataset, the cost functions for all 45 pairwise possible comparisons were computed and visualized to gain insights into their properties. The beampatterns included in this sample dataset were selected to represent beampattern characteristics seen across the full dataset in a qualitative fashion. Specifically, beampatterns were chosen to represent three non- exclusive trends: (i) the presence of single or multiple well- defined lobes, (ii) the presence or absence of large changes in lobe orientation with frequency, and (iii) the presence or absence of pronounced local features like spectral notches. For each comparison within this dataset, a sampled version of the entire cost function was computed (Figure 2.1). The cost function was visualized with a set of isosurfaces. These visualizations showed that the cost functions for all 45 pairwise alignments had the following two properties: (i) each cost function had a unique global minimum and (ii) the local and global minima lay inside a fairly narrow, crescent-shaped subregion of the rotation space. Additionally, it was found experimentally that increasing the p-norm value caused separation and shrinking of the minima regions as visualized by the isosurface. Hence, a p-norm value of 25 was chosen for this reason.

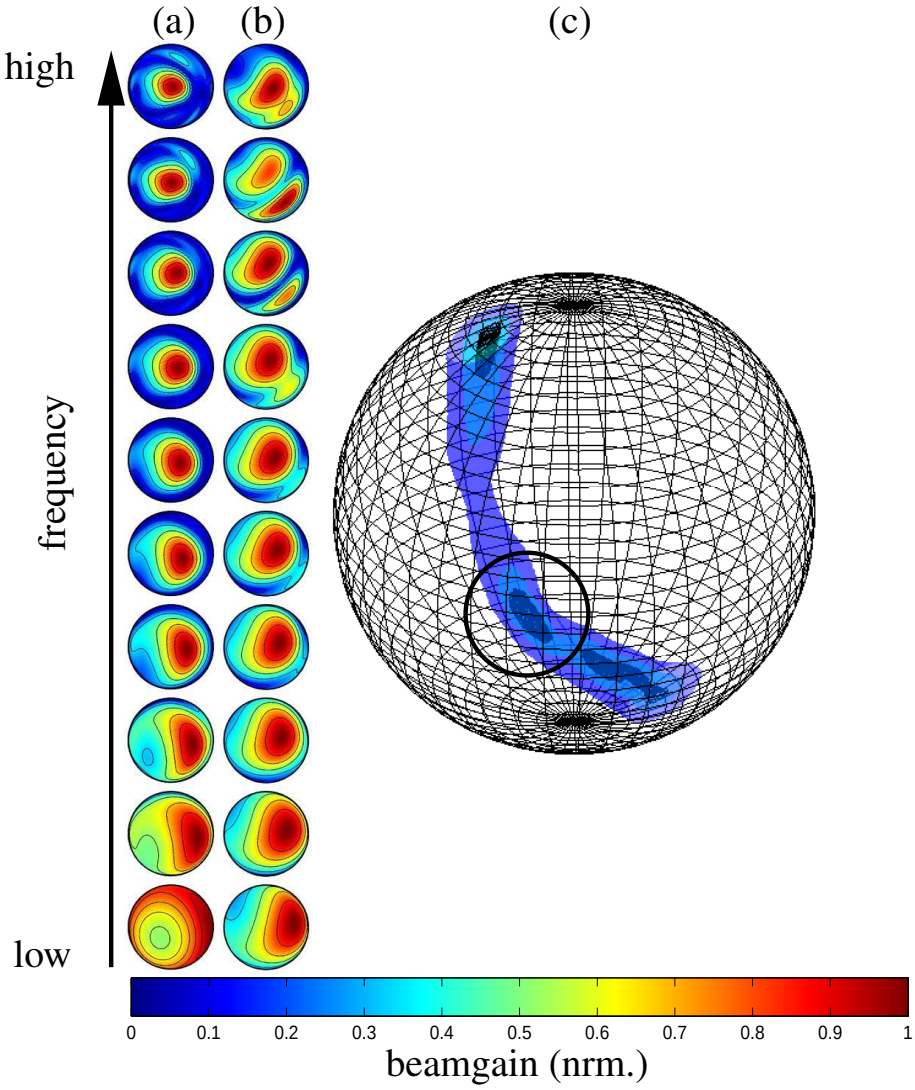

Figure 2.1: Example of pairwise beampattern alignment: (a) fixed Leschenault's rousette beampattern (*Rousettus leschanulti*, emission frequency range sampled from 17 kHz to 34 kHz in equal steps), (b) misaligned Nathusius' pipistrelle (*Pipistresllus nathusii*), sampled at frequencies from 4 kHz to 29 kHz in equal steps) to target beampattern, (c) scalar cost field resulting from alignment of Nathusius' pipistrelle to Leschnault's rousette's beampattern visualized with three isosurfaces representing values of 105 %, 110 %, and 120 % of the global minimum. The location of the global minimum is enclosed by circular marker shown.

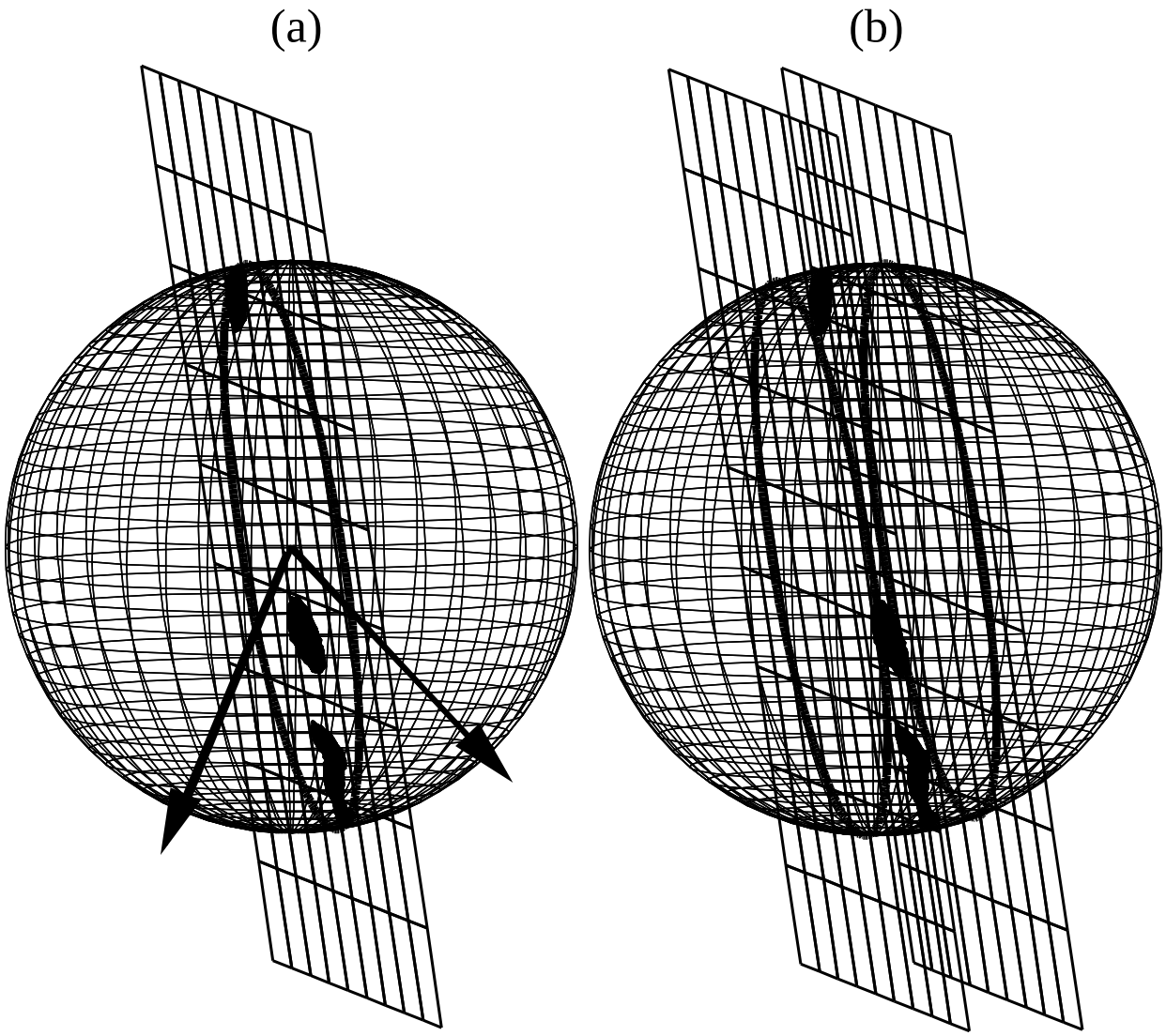

Figure 2.2: Finding a small subspace that contains the global minimum of the beampattern similarity metric (for the two beampatterns shown in Figure 2.1a): (a) bisecting plane between the two beam gain-weighted direction vectors of each beampattern next to the 105 % global minimum cost surface, (b) resulting search space defined by a region bounded by two parallel planes offset from the bisecting plane and the rotation sphere by 20 % of the radius.

2.3.4 Beampattern alignment

The existence of a comparatively narrow crescent-shaped region that contains all the minima of the cost function is a result of the directional nature of the beampatterns. The crescent corresponds to all rotations that produce a significant overlap between the regions of high beam gains of both beampatterns. It was found that the region in the rotation space that produces this overlap can be predicted from an "average direction" of the beampatterns. The average direction of a beampattern was computed as the weighted vector sum of the directions of all sample points on the beampattern. The beampattern gains at the sampling points were used as weights. The rotations that align the two average direction vectors of the two beampatterns define a plan through the rotation space that contains the origin (Figure 2.2a). Within the 45 pairwise alignments in the evaluation dataset, this plane was found to be good predictor for the location of the global minima; in all cases, the global minima fell within $\pm 20\,\%$ of the radius of the region containing all rotations ($180\,^\circ$ maximum) from this plan. As a consequence, the search for the global minimum could be limited to a subset of the rotation space defined by these two parallel planes (Figure 2.2b). Pairwise alignment of beampatterns could then be summarized into a three step procedure: (i) finding the gain-weighted direction vector of each beampattern, (ii) perform an exhaustive search of the rotation subspace defined by the plane that contains all the rotations that contain the two direction vectors, (iii) select minimum found in the exhaustive search to define the rotation in the beampattern alignment. This procedure was applied to a set of 5 beampatterns aligned to a target as shown in Figure 2.3. The target beampattern was the mean beampattern developed from the alignments of

9 of 10 sample beampatterns to the remaining beampattern. The resulting average of the 10 aligned sample beampatterns was used as the target beampattern with which to align all 267 beampatterns.

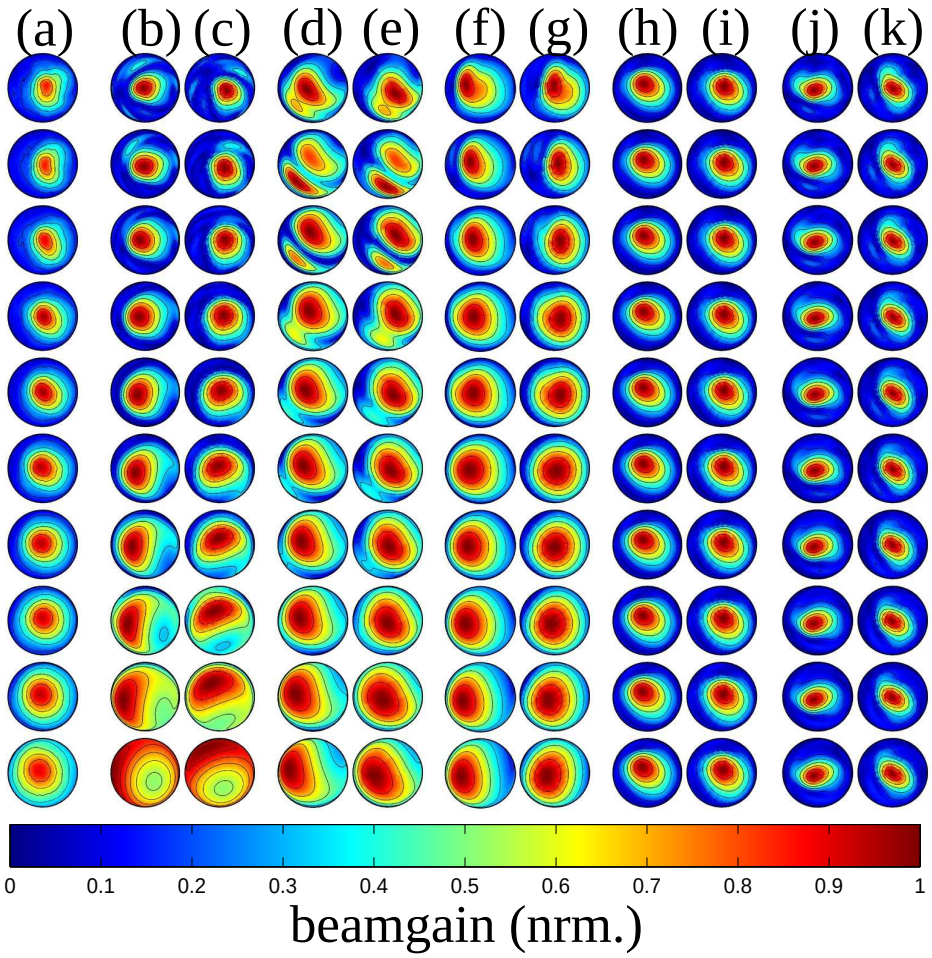

Figure 2.3: Examples of beampatterns aligned to the target beampattern: (a) mean of pairwise alignment of sample beampatterns to Lenschault's rousette or target beampattern, (b) pre-alignment Leschenault's rousette (*Rousettus leschanaulti*) beampattern, (c) beampattern of Leschenault's rousette aligned to the target, (d) pre-aligned beampattern of Nathusius' pipistrelle (*Pipistrellus nathusii*), (e) Nathusiau's pipistrelle aligned to target, (f) misaligned Asian barbastelle (*Barbastella leucomelas*), (g) Asian barbastelle aligned to target, (h) unaligned Big-eared horseshoe bat (*Rhinolophus macrotis*), (i) Big-eared horseshoe bat aligned to target, (j) unaligned Thomas's horseshoe bat beampattern (*Rhinolophus thomasi*), (k) Thomas's horseshoe bat aligned to target.

2.3.5 Beampattern Eigen-decomposition

The aligned beampatterns were downsampled to reduce the size of the covariance matrix from which the principal components are found as eigenvectors. To achieve this downsampling, a simple thresholding scheme was adopted. All sampling points (directions) for which 90 % of the beampattern samples had gain values greater than -6 dB were retained. This resulted in a reduction from the original 3,072 down to 1,978 points. The retained points formed a contiguous region in the "forward" facing direction and the backside of the sphere was hence largely ignored in the analysis. The sampled beam gain values of each beampattern were reshaped into a 19780×1 vector [30, 61]. The resultant unwrapped gain vectors were then averaged across position and frequency to yield a mean beampattern. The zero mean and properly scaled data was then decomposed using single value decomposition (SVD) and related to the principle components of the covariance matrix [23]. The principle component vectors were then reshaped back into the original beampattern format to obtain eigenbeams [30, 61].

To assess whether functional and taxonomic groupings of the beampatterns were distinct in the space spanned by the eigenbeams, the PCA scores were used as feature vectors as input into a support vector (SVM) classifier [4]. The feature vector input into the SVM classifier varied in length with the number of principle components used, and training and subsequent performance of the SVM using a linear kernel was assessed using a leave-one-out training and classification method for each feature vector length. Hence, the reported correct classification rate reported corresponded to the number of sequential eigenbeams for which

the classification was maximum.

The following four largest families in the dataset, Rhinolophidae, Vespertilionidae, Hipposideridae, and Phyllostomidae were considered for the taxonomic classifications. Classification experiments were carried out for the following pairings: (i) emission versus reception beampatterns in the Rhinolophidae and Hipposideridae (lumped into one taxonomic group), (ii) Rhinolophid and Hipposiderid versus Phyllostomid emission beampatterns, and (iii) Rhinolophidae and Hipposiderida versus Vespertilionid reception beampatterns. The separation of the same groups has been previously studied in a space spanned by the coefficient of a spherical harmonics decomposition [36].

2.4 Results

The rank of the beampattern covariance matrix was found to equal the number of beampatterns in the dataset (267). Hence, decomposition of the beampattern covariance matrix yielded 267 eigenvectors with non-zero eigenvalues. When projected back into the original beampattern coordinate system, the resulting eigenbeams consisted of regions with positive and negative gain.

The mean beampattern and the eigenbeams displayed clear non- random trends. The mean beampattern consisted of a single symmetric lobe, Figure 2.4(b). As frequency increased, the mean beampatterns principle direction did not shift, Figure 2.4(c), but the beamwidth decreased 50 % of the first frequencies beamwidth, Figure 2.4(a).

The first 12 eigenbeams captured two thirds of the variance around the mean while 73 eigenbeams were needed to capture 90 % (Figure 2.5).

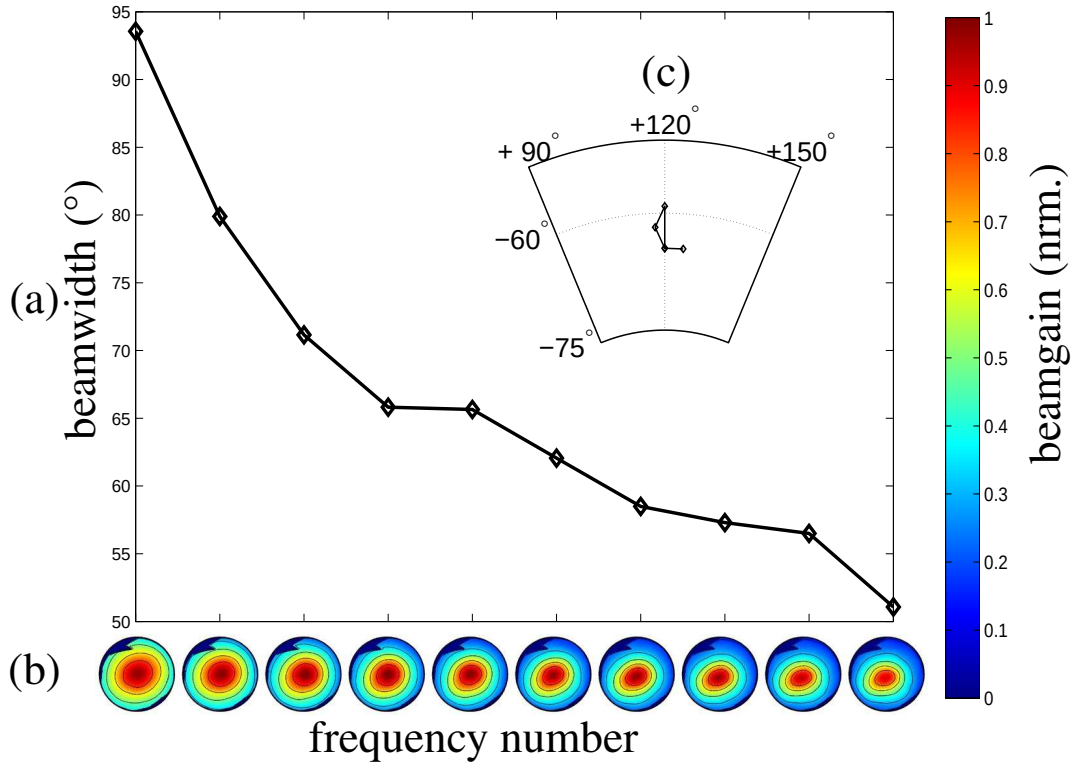

Figure 2.4: Mean beampattern as a function of frequency: (a) the mean beampattern for increasing frequency from left to right. (b) beamwidth as a function of frequency (c) center position of main lobe with increasing frequency.

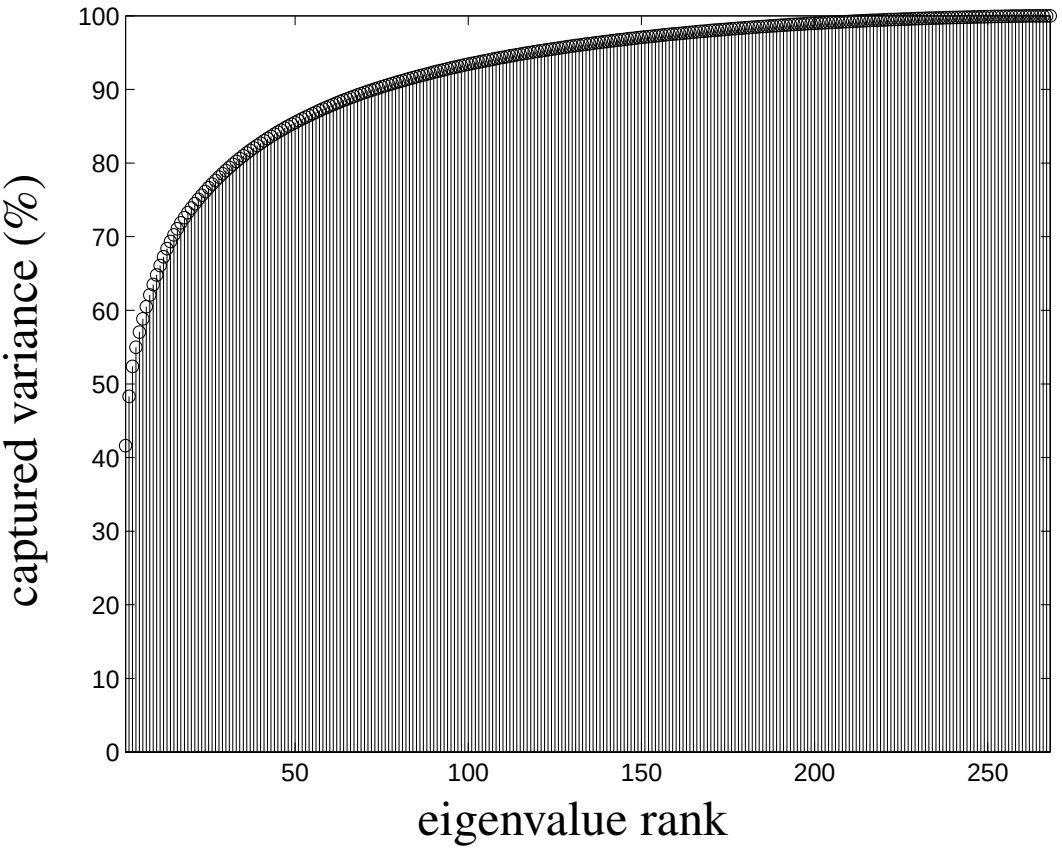

Figure 2.5: Cumulative portion of sample variance captured by increasing rank eigenbeams.

The first three eigenbeams impacted the weighting between the center and the surround of the mean beampattern's principal direction (Figure 2.6). The first eigenbeam strongly affected the beamgain in the surrounding region (with a positive or negative sign) but not at the center where the eigenbeam gain was close to zero. If the first eigenbeam is added to the mean with a negative weight, it uniformly narrows the resultant beampatterns across all directions and frequencies (Figure 2.7a). Conversely, for positive weightings, the resultant beampatterns uniformly expand.

The second eigenbeam shared the center-surround geometry of the first eigenbeam but with opposite sign between high and low frequencies. Hence, adding the second eigenbeam to the mean beampattern emphasizes the surround at high frequencies and suppresses it at low frequencies or vice-versa. Adding the second eigenbeam to the mean beampattern for a positive weight, widens the center lobe at high frequencies while suppressing the center region at low frequencies (Figure 2.7b). Unlike the first and second eigenbeam, the magnitude of the third eigenbeam was largest at the center and close to zero in the surrounding region. Consequently, when added to the mean beampattern, third eigenbeam for negative scalings suppresses the center region (Figure 2.7c). Starting with the 4th eigenbeam, the eigenbeams started to directionally shift principle directions with frequency and break up into multiple lobes (Figure 2.6).

Functional (emission versus reception) and taxonomic beampattern groups showed separation in a low dimensional space spanned by the first few eigenbeams. This was evident in the two dimensional spanned the first two eigenbeams (Figure 2.8).

A linear support vector machine (SVM) classifier was able to achieve a high classification rate for both taxonomic and functional groups beampatterns.The best classification performances were observed in comparatively low dimensional eigenbeam spaces. For emission versus reception beampatterns, the best observed correct classification rate (85 %) was achieved at 14 eigenbeams. Within the Rhinolophidae and Hipposideridae, the correct classification rate for emission versus reception beampatterns was at 92 % based only on 3 eigenbeams. Rhinolophid and Hipposiderid emission beampatterns could be correctly distinguished from

those of the Phyllostomids 76 % using 17 eigenbeams. For reception beampatterns, the correct classification rate of Rhinolophid and Hipposiderid versus Vespertilionid was 95 % for 14 eigenbeams.

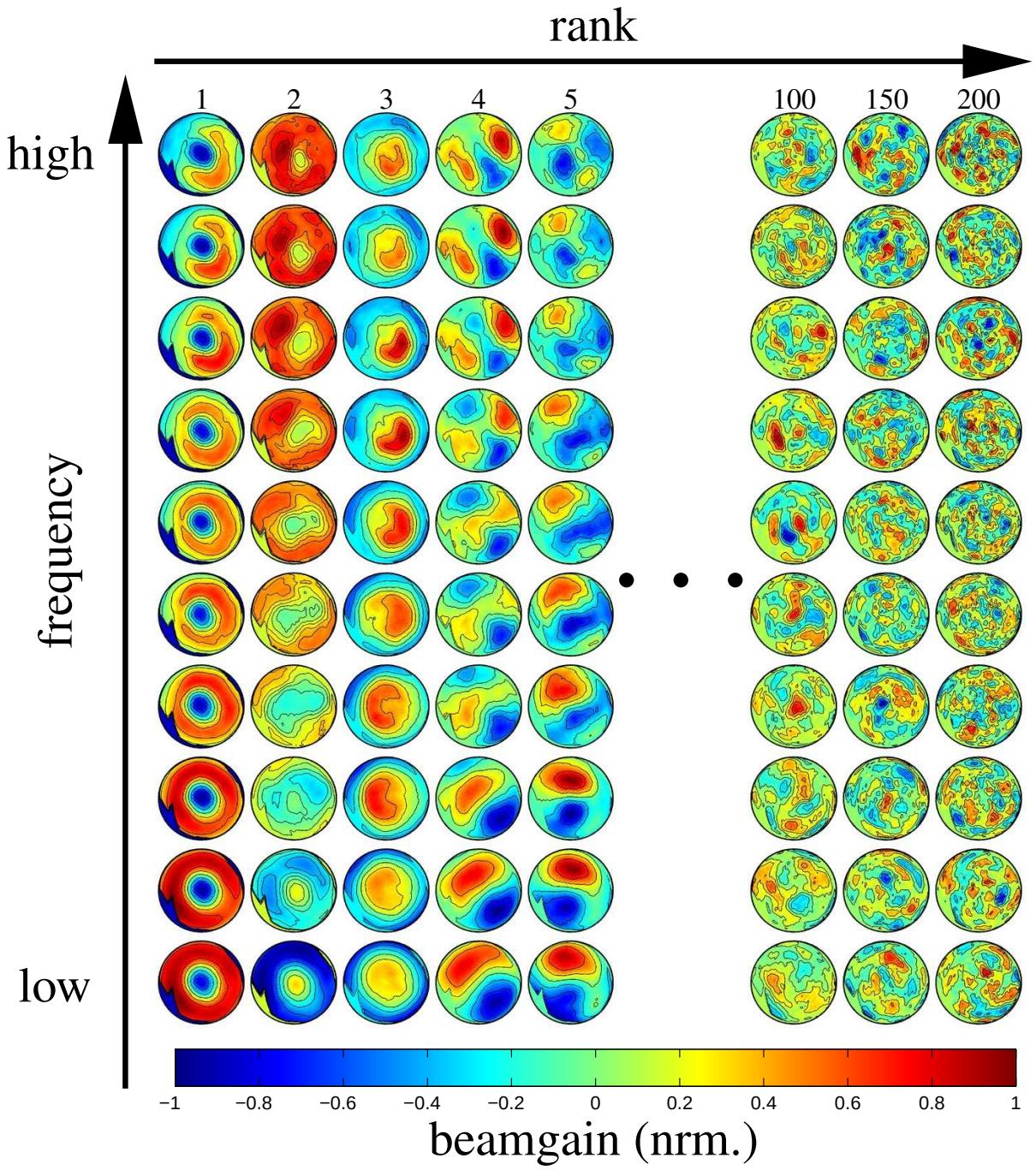

Figure 2.6: Eigenbeams (eigenvectors of the beampattern covariance matrix mapped back into the original beamspace) sorted by decreasing eigenvalue.

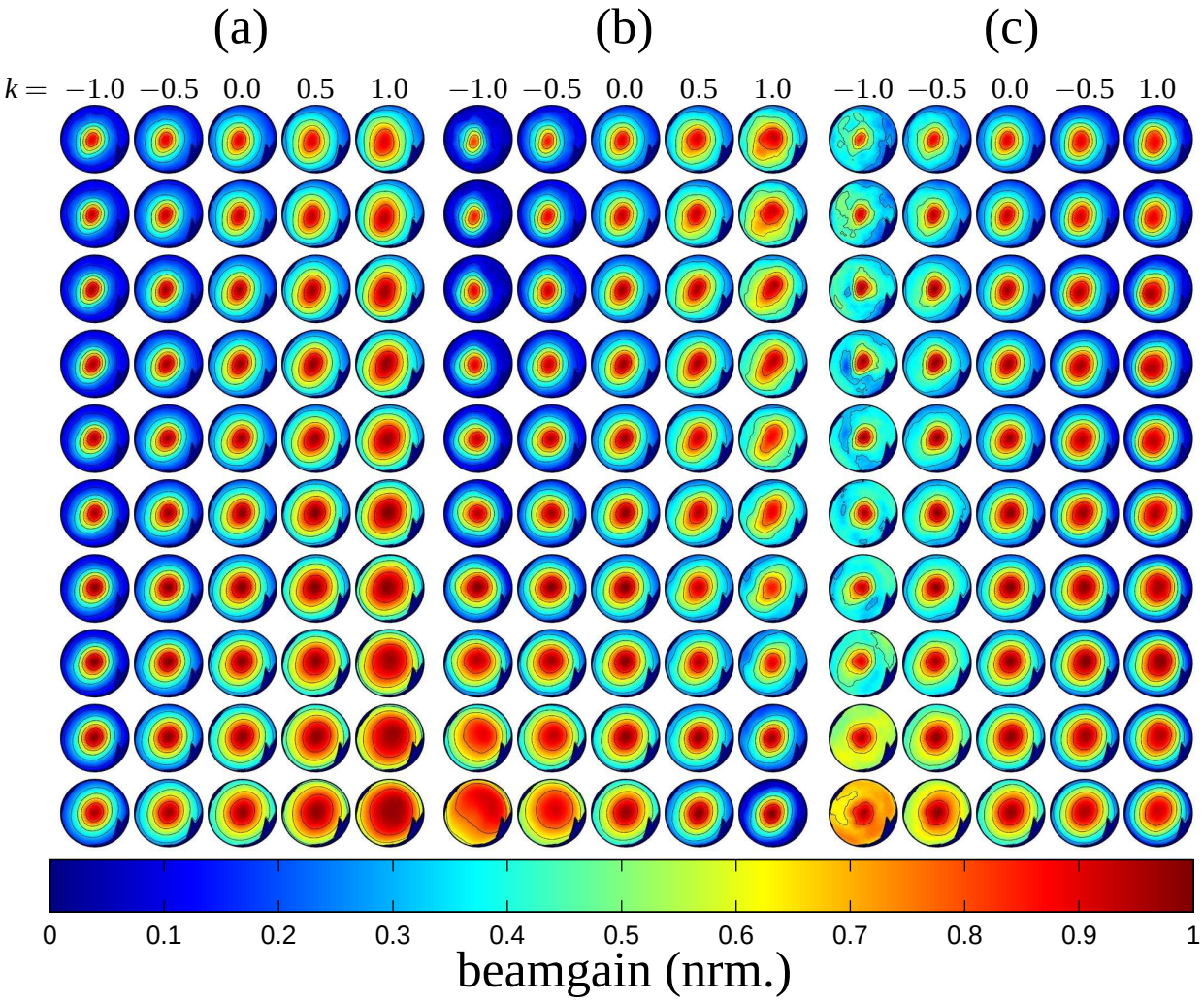

Figure 2.7: Effect of first three eigenbeams, $kG_i(\theta, \phi)$, when added to mean beampattern, $G_m(\theta, \phi)$, for $k \in \{-1.0, -0.5, 0.0, 0.5, 1.0\}$: (a) eigenbeam 1, (b) eigenbeam 2, (c) eigenbeam 3.

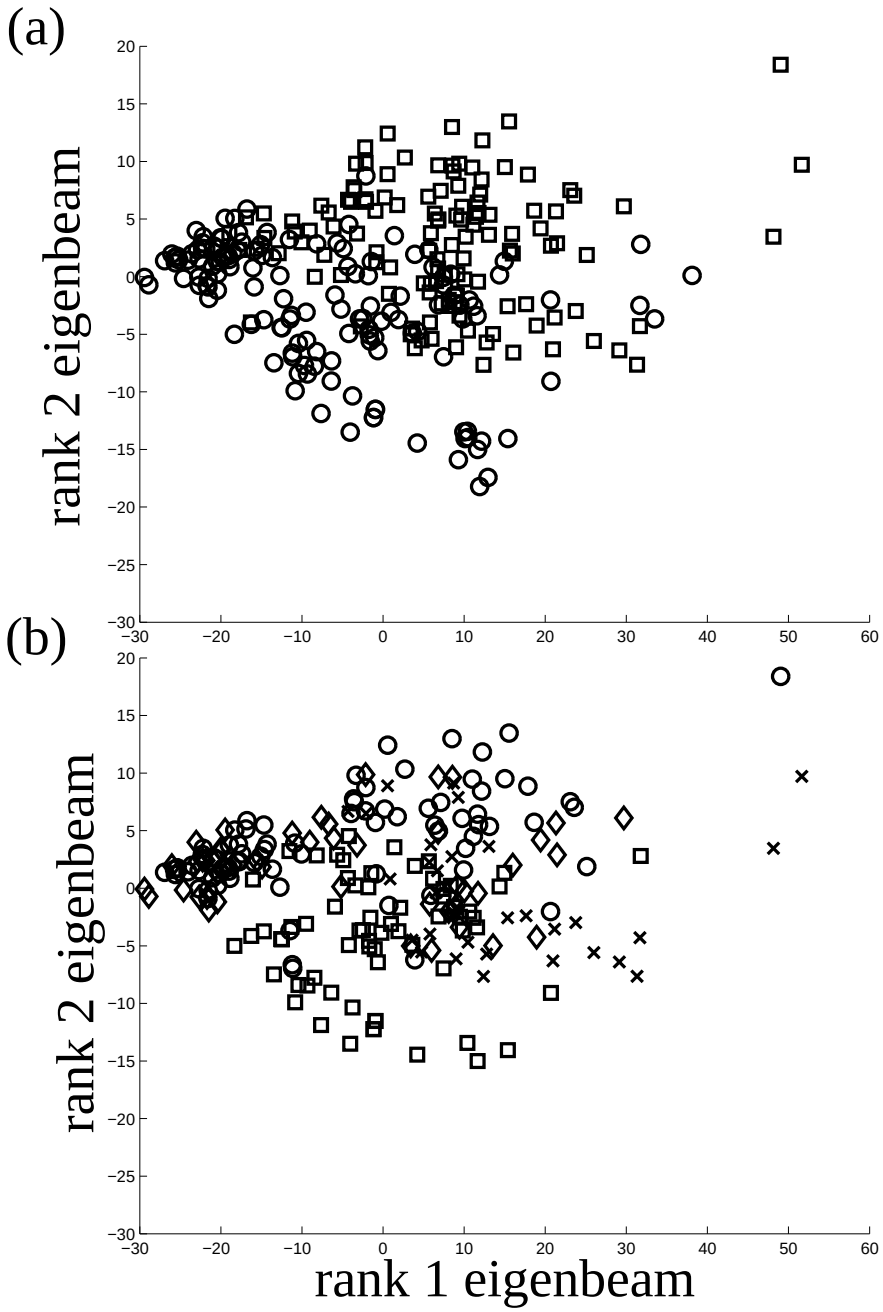

Figure 2.8: Distribution of beampattern samples in the space spanned by the first two eigenbeams: (a) scores of emission and reception beampatterns: pinnae (circles), noseleaves (squares), (b) scores of four largest family groups: old world leaf-nosed bats (*Hipposideridae*, diamonds); leaf-nosed bats (*Phyllostomidae*, X), horseshoe bats (*Rhinolophidae*, circles), vesper bats (*Verspertilionidae*, squares).

2.5 Discussion

This work presents analysis of the interspecific variability in bat biosonar beampatterns through principal component decomposition of 267 complete beampattern geometries from 98 species. This analysis was enabled by two key findings: i) beampatterns can be aligned uniquely using a p-norm cost metric and ii) it is possible to delineate a restricted subspace containing the optimum alignment.

The analysis of the aligned beampatterns reveals readily interpretable trends in biological variability. The mean beampattern is simple and reflects the basic physical relationship between aperture size, wavelength, and beamwidth. As the frequency increases, the width of the mean beampattern decreases. Like the mean beampattern, the first three eigenbeams show a simple pattern of center-surround organization. The first and third eigenbeam can be seen as a complimentary pair that influences the center or surround separately but independent of frequency. The second eigenbeam introduces a frequency dependency into this center-surround organization. Since changes to the center-surround organization also affect beamwidth, this finding is consistent with the observation that beamwidth is a major factor in beampattern variability and categorical differences [36].

The eigenbeam space not only captures the overall variability but also the categorical differences between functional and taxonomic groupings of beampatterns. Nevertheless, nearly complete capture of the variability requires a large number of eigenbeams. This finding differs notably from to the results obtained in the prior eigen-analysis of bat pinna [30] where

a much smaller number (32) of eigenears captured 90 % of the variability. This discrepancy could be the result of differences in sample size (100 pinna shapes from 59 species versus 267 beampatterns from 98 species). Alternatively, it could reflect an asymmetry between pinna shapes and beampatterns. Small changes in the pinna geometry could trigger large changes in beampatterns.

Future work is needed to further elucidate the relationship between eigenears and eigenbeams. Due to the complexity of the acoustic relationship between pinnae and beampatterns, exploration of this relationship is not trivial. Joint decomposition of pinna and beampattern space could result in insights that could not be predicted either domain. [23]

Chapter 3

A design for a dynamic sonarhead inspired by horseshoe bats

3.1 Executive Summary

Horseshoe bats (Rhinolophidae) are noteworthy because of their sophisticated pinnae and noseleaf shapes surrounding the emission and reception apertures of their biosonar system. During biosonar operation, both the noseleaf and pinnae have been shown to actively deform. Since both the noseleaf and pinnae shape and dynamic motion directly affect the properties of the animal's biosonar system, this work mimics horseshoe bat shape and motion with the goal of developing a platform to study the dynamic sensing principles horseshoe bats employ. To this end, two robotic devices were developed to mimic the dynamic emission

and reception characteristics of horseshoe bats. The shapes of both the noseleaf and pinnae with different local feature combinations were modeled and manufactured out of silicone. The noseleaf was mounted to a platform called the dynamic emission head to independently actuate three surface elements of the noseleaf similar to motion observed *en vivo*. Similarly, the pinnae were mounted to a platform called the dynamic reception head to bend the pinnae similar to motions observed *en vivo*. Motion of the noseleaf and pinnae were synchronized to the incoming and outgoing sonar waveform, and the joint time-frequency properties of the noseleaf and pinnae local feature combinations and combinations of the pinnae and noseleaf thereof were systematically characterized across spatial direction. Amplitude modulations to the outgoing and incoming sonar pulse information across spatial direction were observed in all pinnae and noseleaf local shape feature combinations. Peak modulation variance generated by motion of the pinnae and combinations of the noseleaf and pinnae approached a white Gaussian noise variance bound. However, it was found the dynamic emitter generated less modulation than either the combined or reception scenarios.

3.2 Introduction

Bat biosonar and engineered sonar systems share the same fundamental operating principle. Both transmit energy into the environment to infer information from the echo. However, the approaches taken to achieve this goal are quite different. Technical sonar solutions distribute sensors over an aperture because combining information from sensors across the

aperture allows information about the impinging wavefront to be inferred [62]. Increasing the aperture size to many times the wavelength improves angular resolution at the cost of more sensors and large mechanical size [68]. In contrast, bats have very few sensing elements, two, and an aperture size a few wavelengths of its operating frequency. Nevertheless, bats do not appear to sacrifice performance despite their size. For example, big brown bats (*Eptesicus fuscus*) were shown to discriminate between targets arranged 1.5 ° apart [27]. If a sonar array with an equivalent resolution to the angular acuity of a big brown bat was constructed, the result would be 80 times the size of the animal and 2 orders of magnitude more elements [14].

3.2.1 Biological Sonar: Horseshoe bats

What bats lack in sensor elements and mechanical size, it may be hypothesized they make up for in shape complexity surrounding their emitting and receiving apertures. Indeed, significant biological investment in biodiversity to the outer shapes surrounding the biosonar emission and reception apertures seems to be the hallmark of bat biosonar [30, 2]. Bats emit sound orally or nasally [1]. In nasal emitting bats, the sound emission site are often surrounded by intricate baffles termed noseleaves which serve to shape the outgoing emitted sound [74, 63, 73, 52]. Mouth gape and shape structures surrounding orally emitting bats may serve a similar function to the noseleaf [25]. For all echolocating species, bats receive biosonar information through structurally complex pinnae which give the animal directional hearing [43, 3].

Most species' pinnae and noseleaf baffles around the emission aperture are static during biosonar operation; however, horseshoe bats (family Rhinolophidae) feature active shape dynamics to the noseleaf and pinnae [16, 48, 10, 19, 13]. During pulse emission, the noseleaf surface immediately surrounding the nostrils termed the anterior leaf, Figure 3.1, deforms inwards [10]. Additional anterior flexion of the lancet structure above the nostril aperture has been shown to be timed to the pulse emission [19]. During prey capture, horseshoe bats are reported to change the width of the emitted sound beam [32]. Motion of the noseleaf is speculated to be the driving mechanism [32]. Horseshoe bats exhibit fast motion of the pinnae during biosonar operation [16, 48]. This motion is hypothesized to assist the animal in localization tasks. For example, during active obstacle avoidance experiments, horseshoe bats with enervated pinnae avoid vertically arranged targets less well than untouched specimens [35].

While it is clear dynamic shape changes manipulate the properties of the bat's biosonar, it is less understood how dynamic shape change benefits biosonar operation particularly in natural environments. Horseshoe bats hunt insects close to vegetation using long duration constant frequency calls starting and terminating with a brief low bandwidth frequency modulation. Insects add motion information to the long CF component of the echo which in part helps separate echo clutter from prey generated cues [53, 28]. However, the benefit to adding self generated motion to dynamic information returning from the environment is unknown. Furthermore, narrowband, constant frequency (CF) calls lack bandwidth other species might use to localize [3].

Beampatterns describe the interaction between the noseleaf and pinnae and outgoing and incoming acoustic waves through diffraction. Hence, properties of a noseleaf and pinnae are often described as a joint time-frequency response functions that vary with spatial direction. Beampattern properties of the noseleaf and pinnae along different deforming conformation states have been predicted numerically. In all cases, interplay between local shape features on the shape structures and motion of the shape elements generated strong systematic changes to the beampattern properties [19, 18, 13]. Combination of the predicted reception and emission beampatterns with rigid rotations of the pinnae showed motion and shape features coordinated to improve localization and clutter rejection in simulation [64].

3.2.2 Biomimetic Approach

As a biological system with sophisticated biosonar properties, horseshoe bats represent a potentially rewarding avenue for biomimicry. Since outer shape dynamics in bats are governed by physical relationships between sound and outer noseleaf and pinnae shapes, studying a biomimetic prototype mimicking the biological system is not only a more reliable approach than using live animal but also less limited than a numerical simulation. Consequently, this work has taken a step towards developing a biomimetic sonarhead closely modeled after the horseshoe bat.

Dynamic acoustic properties of the horseshoe bat noseleaf and pinnae have been studied separately using biomimetic prototypes. Pannala et al. [41] constructed a model of the pin-

nae with selectable local shape features. Sharp changes to the beampattern properties were observed for combinations of local shape features over a deforming motion pattern [41]. Similarly, Fu and Müller [70] suggested a simple shape model of the noseleaf's anterior leaf and emission aperture and also demonstrated time variant effects to the emission beampattern. In both, the beampattern properties were measured along static conformation steps over the baffle's range of motion.

Several robotic systems combined both shape and/or motion elements to make complete bioinspired bat sonarheads. Walker et al. [66] developed a simple model of the reception dynamics in horseshoe bats by treating the rotating pinnae as rotating circular receiver elements. Amplitude modulation cues generated from rotating the two receivers out of phase were used to localize sounds in the vertical direction [66]. Similarly, Kuc [26] developed a robotic sonar which used scanning of the receivers relative to the target for localization. The receiver and transmitter element like Walker's were circular ultrasonic transducers. Later, the CIRCE biomimetic robotic platform used a similar design to Walker et al. [66] but added different pinnae shapes to the receiving elements [46, 40].

From these prior developments, several requirements to the design and subsequent characterization of the biomimetic sonarhead were followed. First, motions of pinnae and noseleaf elements of the sonarhead were kept to deforming motion patterns qualitatively similar to those observed *en vivo*. Past work suggests pinnae rigidly rotate during operation [66]; however, it also has been observed pinnae motion patterns include deforming motion patterns [72, 13]. This work used the deforming motion pattern and pinnnae described by Pannala

et al. [41] as a reference . Second, characterization of the pinnae and noseleaf acoustic properties were analyzed over continuous motions rather static imaging of the properties over static conformation stages. This bypasses any limiting assumptions about continuity between conformation stages and captured any fast time dynamic effects present in the system [34]. Finally, since dynamics effects cascade from the emitter back to the receiver, splitting dynamic the emission and reception into separate devices allowed individual characteristics be measured. Combining the non-collocated dynamic devices is accomplished by making the assumption that echoes returning an idealized point target ensonified by a dynamic emitter preserve any time-variant characteristics generated motion of the dynamic emitter baffl. Hence, the coupled emission-reception time dynamic response can be measured by pointing the dynamic emitter device at the dynamic receiver device and measuring the dynamically received response from a dynamically emitted signal.

In the following sections, two robotic devices carefully mimicking the shape and motion patterns of the horseshoe bat are developed. The goal of this work is to first develop platforms to dynamically emit and receive sonar information similar to the horseshoe bat's sonar system and demonstrate this developed method has strong time variant acousti cproperties (if any). Since noseleaf and pinnae shapes influence the dynamic properites of the emitter and receiver devices, different local shape features on the baffles are constructed and the relative merit between shape for fixed motion patterns evaluated.

3.3 Methods

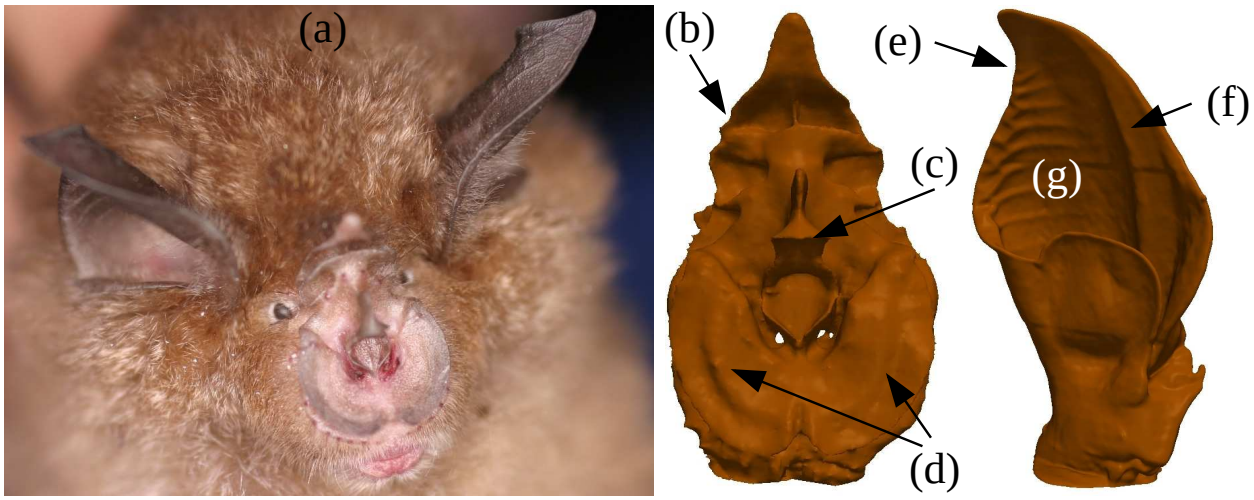

Figure 3.1: Horseshoe bat noseleaf and pinnae local shape features: (a) greater horseshoe bat (*Rhinolophus ferrumequinum*) specimen used as a reference in this work (b) noseleaf lancet furrows (c) sella (d) anterior plates surrounding the "U" shaped emission aperture (e) incision [41] (f) spine structure along the anterior edge or leading edge of the pinnae (g) washboard ridge pattern along the posterior edge

3.3.1 Biomimetic dynamic emission

The biomimetic noseleaf outline profile matched approximately the reference noseleaf profile using a composite of straight line and circular shape primitives, Figure 3.1. From base of the anterior plate to the tip of the lancet, the noseleaf was 45 mm tall and at its widest, 35 mm - corresponding to a 2.5 scaling factor applied to the reference noseleaf outline. Nostrils were positioned 1/3 the total height up from the base of the noseleaf and were symmetric to the

median plane.

The nostril emission apertures through the material thickness of the noseleaf were formed by smoothly lofting the two 5 mm diameter circular profile apertures to half "U" shaped slits on the front surface of the noseleaf. The nostril emission apertures were made wider than the 2.5 scale dimensions in order to improve sound amplitude transmitted downrange. A bowl shaped depression was added to the anterior plates to mimic the general concave structure of the noseleaf.

Two different local shape features were added to the noseleaf: (i) a sella structure which extended over the nostrils at a 45 ° angle, Figure 3.1c & 3.2f and (ii) lancet furrows of 5 mm depth and 3 mm opening width, Figure 3.1f & 3.2b . Noseleaf baffle feature combinations were generated independently by adding or removing the furrow and sella from the noseleaf, Figure 3.2f.

All noseleaf baffles were designed in CAD software (Autodesk Inventor 2015) and different noseleaf feature combinations were 3D printed. Molds of the 3D printed noseleaves were made, and flexible noseleaves were cast out of silicone (Ecoflex 30-30, Smooth-On Corp.). Two biomimetic noseleaf baffles were selected for later acoustic characterization: (i) a noseleaf with lancet furrows and a sella and (ii) a noseleaf without either aforementioned features Figure 3.2e.

Motions elements were added to the emission head to mimic anterior leaf and lancet motions observed in horseshoe bat noseleaves [10, 19]. Each lateral anterior plate was pushed forward

from behind using planar four bar mechanisms and servo motors in-line with the transverse plane, Figure 3.2a. This motion increased the concavity of the anterior plate surrounding the emission apertures symmetrically with respect to the median plane; however, since each anterior plate was driven separately, median plane asymmetric motions of the anterior plate were possible. Within this work, only median plane symmetric motions of the anterior plate were considered. Lancet flexion was increased by a pushing on the back surface of the lancet using a similar four bar mechanisms and DC servo motor in-line with the assemblies median plane, Figure 3.2d. The dimensions of the driving and driven linkages on all four bar mechanisms had approximately $1:1$ length ratios to directly translate angular displacements at the servo motor to equivalent angular rotations at the output. The two anterior leaf actuating mechanisms were driven by brushed DC servo motors with quadrature encoders (Maxon ReMax29 & MR512 512 cpt encoder, Maxon Motors) while the lancet motor was driven a brushed DC servo motor with an encoder (Maxon RE25 & HEDL 500 cpt encoder, Maxon Motors).

Two electrostatic transducers driven in parallel (Series 600, Senscomp) generated sound output between 20 and 100 kHz. Conically shaped waveguides were used to transition each of the 38 mm diameter transducers to the nostril emission apertures of the noseleaf, Figure 3.2c. Each cone waveguide was 100 mm in length, and the two cones were positioned side-by-side such that there was a cone outlet per nostril. A power amplifier (AA-301HS, AA Lab Systems) boosted the signal generated by the data acquisition system output to drive the transducers and a dedicated 200 V DC power supply to biased the driving signal.

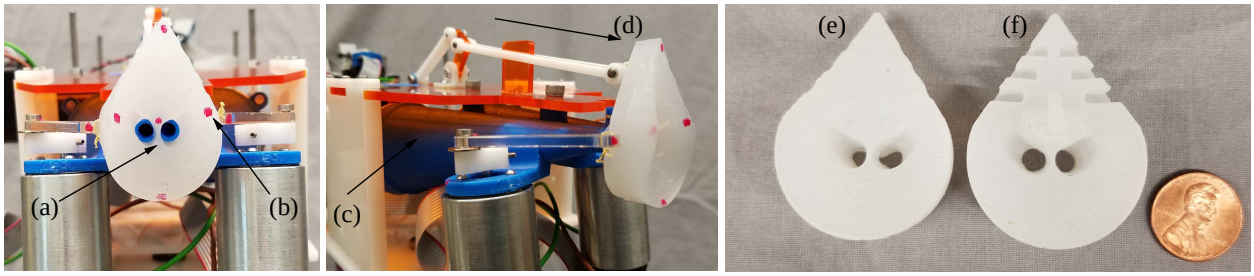

Figure 3.2: Biomimetic dynamic emission device with interchangeable noseleaf baffles: (a) emission aperture (b) anterior plate and driving linkage (d) forward lancet flexion driving linkage (e) noseleaf baffle without lancet furrows and sella (f) noseleaf prototype with lancet furrows and sella projecting over emission aperture, see Figure 3.1b,c for reference

3.3.2 Biomimetic dynamic reception

A smooth reconstruction of a male greater horseshoe bat (*Rhinolophus ferrumequinum*) specimen's pinnae, obtained in Shandong Province, China, was made by matching a smooth spline surface to a μCT reconstruction (23.8 μm) of the reference pinnae surface in Autodesk Maya [22], Figure 3.1c. By matching a smooth surface to the inner pinnae surface, small geometric details and local shape features were ignored, and a pinnae without any local shape features made. The pinnae were 2.5 scale versions of the reference pinnae which resulted in an overall height of 65 mm. The material thickness added to the inner surface was 3 mm.

Three local shape features were added back to the pinnae using Panalla et al. as inspiration, Figure 3.3b , [41]. First, a repeated pattern of 5 ridges moving along the posterior edge of the pinnae towards the tip of the pinnae was added, Figure 3.1g & 3.3(e,i). The ridge

pitch was a fixed 5 mm distance while the height from the inner surface of the pinnae was adjusted in 0 , 2 , and 5 mm increments. Second, a raised spine structure was positioned near the anterior edge of the pinnae and adjusted in 0 and 5 mm height increments, Figure 3.1f & Figure 3.3e. Placement of the spine and ridge local shape features were kept qualitatively similar the reference pinnae. Finally, the posterior edge of the pinnae was modified either have an incision profile like the reference pinnae shape or a posterior edge profile similar to the leading edge of the pinnae, Figure 3.1e & Figure 3.3(e,ii)

Subsequently, 12 combinations of ridge, spine, and posterior edge profile modifications were generated for later acoustic characterization, Figure 3.3e. Like the noseleaf, each individual pinnae local feature combination was 3D printed and a pinnae cast out of flexible silicone (Dragon Skin 30, Smooth-On Corp.). The ear canal was formed by punching an 1/8 ” diameter hole at the base of the pinnae and coupled to a microphone, by sliding the pinnae over a cylindrical tube terminating at the microphone sensing aperture (Dodotronic momimic, Knowles SPU0410LR5H-QB), Figure 3.3d.

Each pinnae was independently actuated, Figure 3.3c. For both pinnae, a servo motor (Maxon RE25 & HEDL encoder combo, Maxon Motors) with a simple cam directly attached to the servo shaft bent the pinnae from an upright neutral state to a bent conformation state, Figure 3.3a,b,c. PVC tape was adhered to the posterior surface of the pinnae to allow the cam to gently slide across the pinnae.

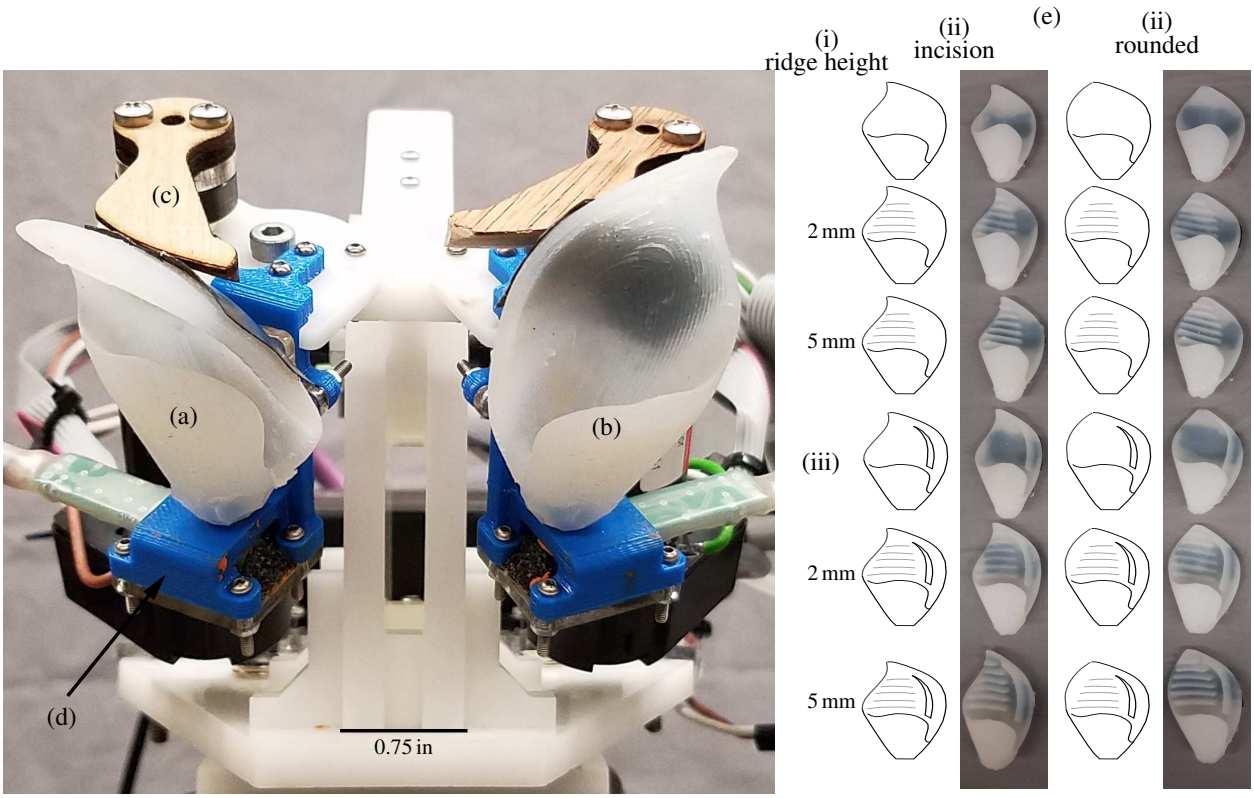

Figure 3.3: Biomimetic dynamic receiver device with interchangeable and dynamically configurable pinnae: (a) pinnae in an bent conformation state (b) sample pinnae in upright conformation stage (c) actuating servo motor and cam (d) coupling between microphone and ear canal of the pinnae (e) left pinnae with 12 different local shape feature adaptations: (i) washboard ridge pattern on posterior edge of pinnae in 0 , 2 , and 5 mm height increments, see Figure 3.1g for reference (ii) leading- trailing edge symmetry, Figure 3.1e (iii) spine structure on anterior edge of pinnae in 0 or 5 mm height increments, Figure 3.1f

3.3.3 Baffle motion integration with sonar function

A system of networked servo control units and an embedded controller (4× Maxon EPOS2 24/2 and EPOSP 24/5, Maxon Motors) were used to coordinate the noseleaf and pinnae motion servo motors. The firmware running on the embedded master control unit acted as a server which synchronously moved the DC servos along user specified motion trajectories on user request. Motion profile trajectories were provided as sequences of position, velocity, and time key points. At the start of a motion sequence, the embedded controller signaled to the data acquisition session on a dedicated digital line. Each servo tracked between reference keypoints using cubic interpolation to a master clock provided by the embedded controller [33]. Acoustic test signals were generated and acquired using a data acquisition card (NI-6351, National Instruments) on a 500 kHz clock. Signal generation and acquisition was triggered on the rising edge of digital signal line between the servo controller and the data acquisition system.

3.3.4 Dynamic baffle beampattern measurement strategy

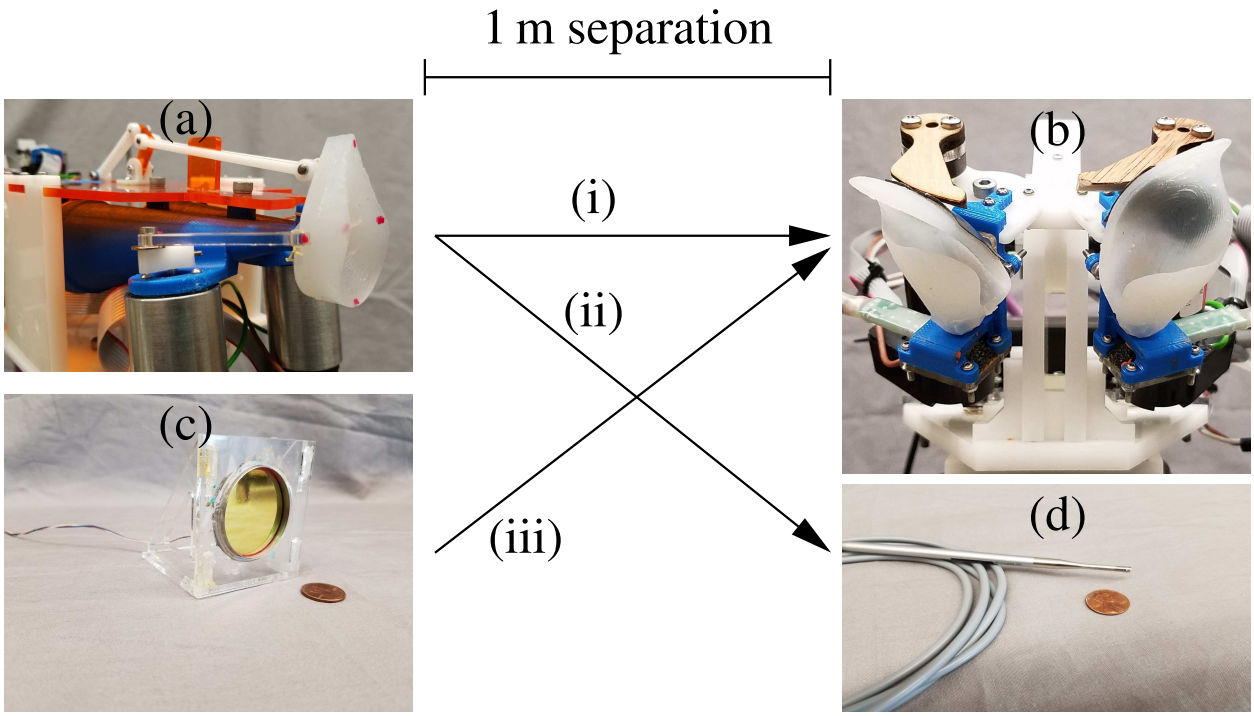

Figure 3.4: Three experimental strategies to measure individual and combined properties of a dynamic emitter and receiver: (a) biomimetic emission device with dynamically deforming noseleaf (b) biomimetic reception device with deforming pinnae (c) ultrasonic speaker (Senscomp Series 600) (d) 1/8" pressure microphone (Brüel and Kjær, Type 4138): (i) combined dynamic emitter and receiver, emitter mounted to pan-tilt unit (ii) dynamic emitter and conventional microphone receiver, dynamic emitter mounted to the pan-tilt(iii) dynamic receiver and conventional speaker, dynamic receiver mounted to the pan-tilt

To measure the individual dynamic acoustic properties of the the emitter and receiver, the dynamic device was placed on a pan-tilt unit (PTU-D48E, FLIR) and a conventional

microphone or speaker element was placed 1 m downrange on a tripod, Figure 3.4(ii)& (iii). Combined dynamic acoustic properties of the emitter and receiver were measured by placing the dynamic receiver on a tripod downrange from dynamic emitter mounted on the pan-tilt, Figure 3.4(i). For all experimental setups, the time domain signal response to a test signal timed to motion the pinnae or noseleaf surfaces(s) was recorded. Hence the dynamic reception characteristics of pinnae mounted to the dynamic receiver device were measured by recording the sound pressure at the base of the pinnae while moving the pinnae timed a test signal emitted downrange from an ultrasonic speaker. Conversely, a microphone downrange of the dynamic emitter recorded the signal transmitted while moving the anterior leaf or lancet surfaces of the noseleaf.

This process was repeated to measure the spatial characteristics of the dynamic emitter and receiver by sequentially scanning the dynamic device mounted to the pan-tilt over a 180 ° azimuth and 76 ° angular sector. 940 positions within the angular sector were sampled using a equal area pixel discretization of the sphere (Healpix resolution level 4) [15]. In the combined emitter and receiver experiment, the noseleaf moved synchronously to the emitted test signal while the pinnae motion was slightly delayed to account for the travel time to the receiver.

At the start of each motion, both the noseleaf and pinnae remained in an neutral conformation states. From there, the baffles moved from an neutral conformation state to a fully deformed conformation state over a 100 ms time period timed to coincide with the emission or reception of the test signal. The test signal emitted and/or lasted 140 ms in duration and

was composed of 30, 32, 40, 50, 60 and 70 kHz superimposed constant amplitude tones. Each emitted signal had raised cosine flanks of 5 ms duration leading and trailing the constant amplitude 140 ms segment of the test signal. Motion of the noseleaf and pinnae baffle were timed to occur within the 140 ms region of the test signal by adjusting the motion trajectory profiles sent to the motion controller.

The time-frequency properties of dynamic noseleaf and pinna were estimated by finding the average envelope of the recorded response at each of the test signal's input frequency bands. Hence, each recorded response was bandpass filtered using a FIR filter with 10 kHz bandwidth tuned to a frequency in the test signal and the envelope estimated using a discrete Hilbert transform. In the case of the 30 kHz input frequency channel, an additional FIR notch filter was applied at 32 kHz. The envelope was then smoothed using an averaging filter kernel length of 1 ms and decimated to a 850 point signal sampled at 5 kHz. From there, the decimated signal was normalized by the peak amplitude value in each individual beampattern. Subsequently, the segment of the recorded response correlating with 140 ms constant amplitude segment of the test signal was extracted, and the variance of this segment estimated after subtracting the mean.

At each spatial sample point, the variance was normalized to a bandlimited, white Gaussian noise (WGN), random variance reference. This value was found using a Montecarlo approach to bootstrap a variance distribution generated bandlimited Gaussian noise. The percentile below which 95 % off all randomly generated variance estimations fell below was used as the *Gaussian reference variance* (GRV).

To generate the bandlimited WGN noise, a FIR filter model (1024 taps) was fit to the magnitude response estimated by taking the maximum magnitude in each frequency bin of all measured 30 kHz amplitude modulations. An ensemble of 180,000 850 point, bandlimited WGN signals were generated by feeding scaled white Gaussian noise through the estimated filter model. The scale factor was estimated by feeding unit white Gaussian noise into the FIR filter transfer function and re-estimating the random amplitude modulation magnitude spectrum. The average DC offset gain between the maximum magnitude spectrum and the re-estimated spectrum was applied as a scale factor to the white Gaussian noise when generating the random ensemble to bootstrap the variance distribution. The signal variance distribution was estimated using Gaussian kernel density estimation.

3.3.5 Baffle surface velocity estimation

Trajectories of fiducial points on sample noseleaf and pinnae baffles during characteristic lancet, anterior leaf, and pinnae motion patterns were reconstructed from stereo video captured at 120 fps. Two GoPro Hero3+ Silver Edition cameras synchronized using a Dual Hero Camera Backpack captured the noseleaf and pinnae motions. At the beginning of each session, the stereo rig was calibrated using still frames of a 7 mm calibration grid moved within the capture volume and and the intrinsic and extrinsic camera parameters estimated [**?**, 20, 6].

5 fiducial points were placed on the noseleaf: 3 along the rim of the anterior plate, 1 at the center of the noseleaf near the emission aperture, and 1 at the tip of the lancet. 12 fiducial

points were placed along the anterior and posterior edges of the pinnae and 1 at a point near the base of the pinnae.

Fiducial points were tracked using an optical flow tracking algorithm manually initialized using a color blob segmentation routine [31]. The pairs of the mean center points in the left and right video after stereo rectification were used to triangulate the 3D position of the fiducial point in the left camera coordinate system. The surface speed vector of the points was then estimated by taking the first time difference of the point trajectory system and taking the magnitude of the velocity vector at each point in time as instantaneous surface speed.

The forward pointing direction of the dynamic emission head was estimated by using fiducial points along the rim of the neutrally deformed anterior plate to define a plane using the center fiducial point at the emission aperture as the origin. The plane normal was taken as the forward pointing direction of the dynamic emitter head and instantaneous angular deformation of anterior plate and lancet subsequently referenced to it.

3.4 Results

3.4.1 Baffle surface motion velocity

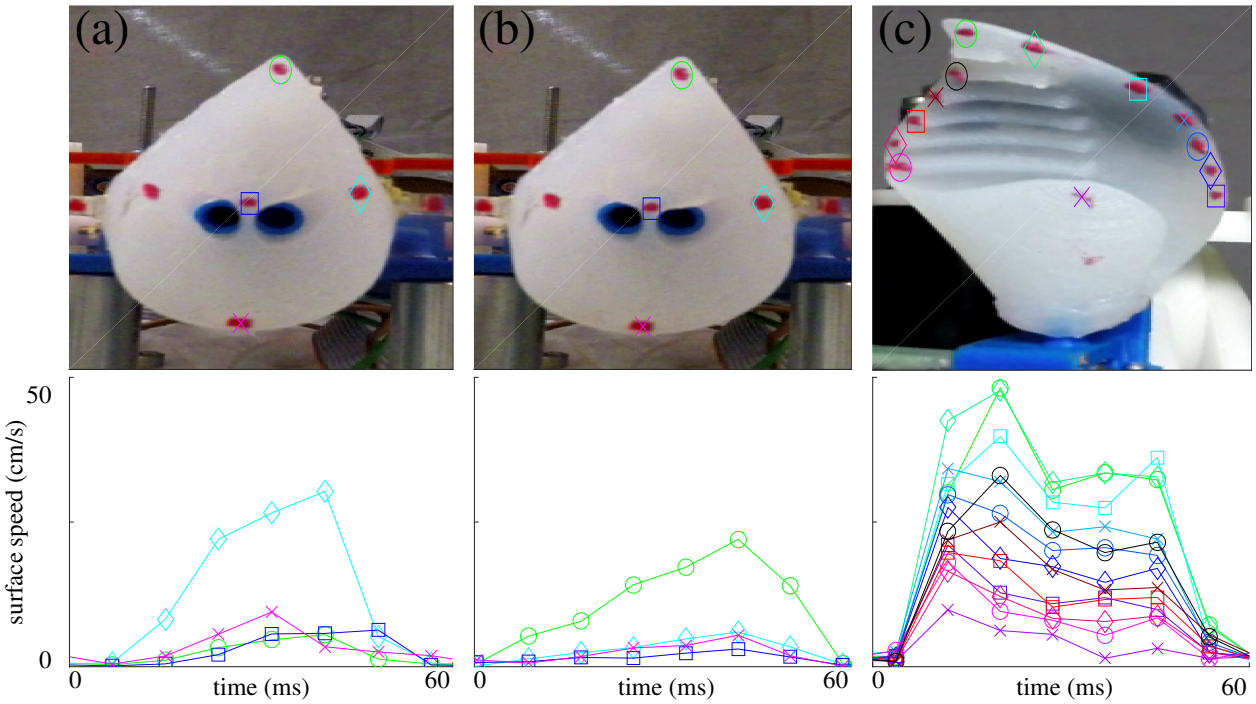

Figure 3.5: Emission and reception baffle motion surface element speeds measured using GoPro stereo camera system at 120 fps for motion going from neutral state to fully deformed conformation bending stage: (a) 2D projection and absolute surface velocity of fiducial markers 2D projection during symmetric anterior leaf concave inwards motion, markers on 2D projections correspond to line markers on time velocity plots below (b) 2D projection of point markers during lancet downwards sweeping motion - below, corresponding noseleaf fiducial points velocity during lancet motion (c) 2D projection and fiducial point absolute velocity for a swept neutral to bent pinnae motion

Over a characteristic anterior leaf motion pattern, the right anterior plate swept an arc distance of 8 mm, Figure 3.5a. During a typical lancet motion, lancet tip moved an arc distance of 6.8 mm, Figure 3.5b. The anterior plate surface reached peak speeds of 30 cm/s while the lancet reach peak speeds close to 25 cm/s. The anterior plate was estimated to deform approximately 27 ° from its neutral position. Similarly, a characteristic lancet deformation bent the surface approximately 15 °. During anterior or lancet motion patterns, small motions occured in the non actuated surface elements of the noseleaf. 2 ° sympathetic angular deformations were observed in both the anterior plate and lancet. Overall motion of the pinnae was consistent with a deformation. Pinnae speeds peaked at 50 cm/s over a 11 mm of arc travel distance. Speeds increased along the surface edges of the pinnae above the cam rotation plane. Points on the leading edge of the were generally faster than points on the trailing edge of the pinnae.

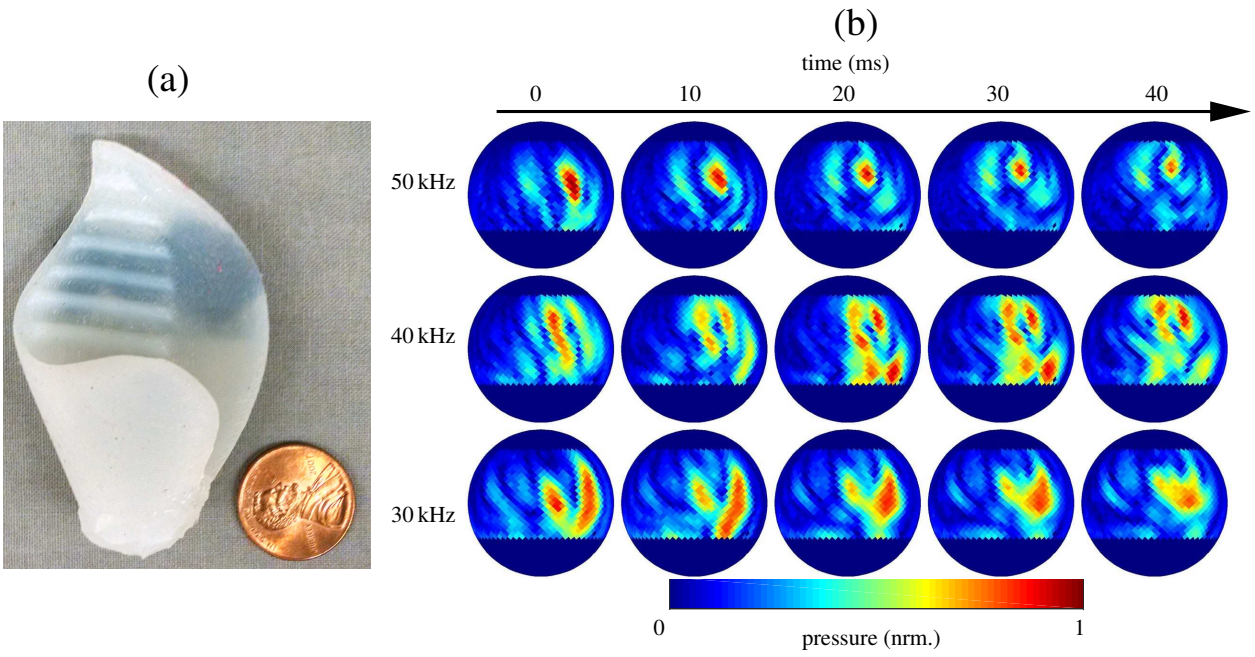

Figure 3.6: Example sound pressure amplitude modulation while receiving a constant amplitude constant frequency multi-sine pulse reception timed upright to bent conformation stage pinnae motion like Figure 3.5c: (a) beampattern snapshots of sound pressure at 30 ,40 , and 50 kHz across time (b) dynamic pinnae element used to measure dynamic properties

3.4.2 Baffle time-variant beampattern properties

All noseleaf and pinnae baffle motions produced systematic amplitude modulations within each frequency band of the emitted test signal, Figure 3.6. For all pinnae and noseleaf shapes, amplitude modulation patterns over spatial direction, strongly depended on time and frequency; however, systematic changes to the beampattern over spatial direction for inclusion of local shapes features and pinnae were not observed. Over time, motion of the

noseleaf and pinnae typically redistributed energy into multiple spatially separated high gain regions (called lobes), combined lobes, and/or manipulated symmetry of the lobes. The only systematic change observed in response to inclusion of local shape features occurred when the lancet of a noseleaf with a sella and lancet furrows was deformed. In this case, energy was redirected to a second lobe pointing below first dominant lobe in time and elevation. Removing the sella and lancet furrows generated no redistribution of energy to the lower lobe for motion of the lancet.

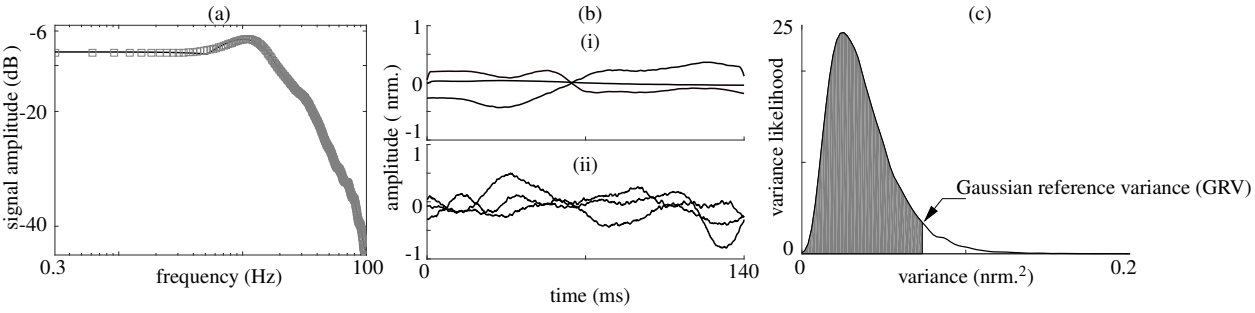

Figure 3.7: Estimation of the bandlimited amplitude modulation variance threshold (BVT): (a) estimation of a noise gain model using measured amplitude modulations around 30 kHz input signal: black line - maximum amplitude frequency response gain at each frequency bin for all receiver, emitter, and combined beampatterns, grey squares - all zero 1024 tap filter fit to measured maximum amplitude modulation spectrum; (b) sample time domain zero mean amplitude modulation realizations selected from measured beampatterns (black) and randomly generated modulations (grey) (c) amplitude modulation variance distribution using noise gain model from (a) to generate 20,000 realizations (d) bandlimited variance threshold at which 95 % of all random amplitude modulations have a value less than the threshold

The 1024 tap FIR filter closely matched the max power amplitude modulation spectrum, Figure 3.7a. This estimated filter model had similar qualities to a low pass filter with a corner frequency of 20 Hz. Furthermore, the bandlimited random Gaussian realizations generated by passing scaled WGN noise through the transfer function showed qualitatively behaviour to measured 30 kHz amplitude modulations, Figure 3.7b. Random Gaussian variance reference value was estimated to be approximately 0.07 , Figure 3.7d.

Similar peak percentages of the random Gaussian variance reference were observed in all reception, emission, and combined beampatterns; however, different local shape feature adaptations generated different spatial distributions of variance and total amounts of variance, Figures 3.8,3.9. On average, 25 % of the total spatial sampling area in the combined and reception patterns was covered by dynamic modulations greater than 5 % of the random Gaussian variance reference. Only two pinnae feature combinations had peak amplitude modulations above 95 % of the random Gaussian variance reference. Both pinnae had 2 mm ridge local features and incision or rounded trailing edges. In these two pinnae, 0.5 % of the total surface area reached above 95 % of the random Gaussian variance reference.

In general, the amount of observed dynamic change in the emission patterns was less than that of the combined and receiver patterns. Only 12 % on average of the total surface areas was covered by modulations above 5 % of the random Gaussian variance reference. Emission patterns did not reach above the 40 % of the random Gaussian variance reference for more than 0.5 % of the spatial area. Peak combined noseleaf and pinnae amplitude modulations reached similar dynamic levels as the noseleaf but covered twice the area (1 %) as the noseleaf

at for the same 40 % dynamic reference variance threshold.

Considering the average variance over all spatial positions, all dynamic emission, reception, and combined beampatterns had greater average signal change compared to static baffles ($p < 0.001$, right tailed t-test) Figure 3.10. In general, the receiver and combined patterns had greater average dynamic change than the emission pattern. However, it should be noted the number of reception and noseleaf combinations considered for each category baffle characterization category varied between 4 and 12 .

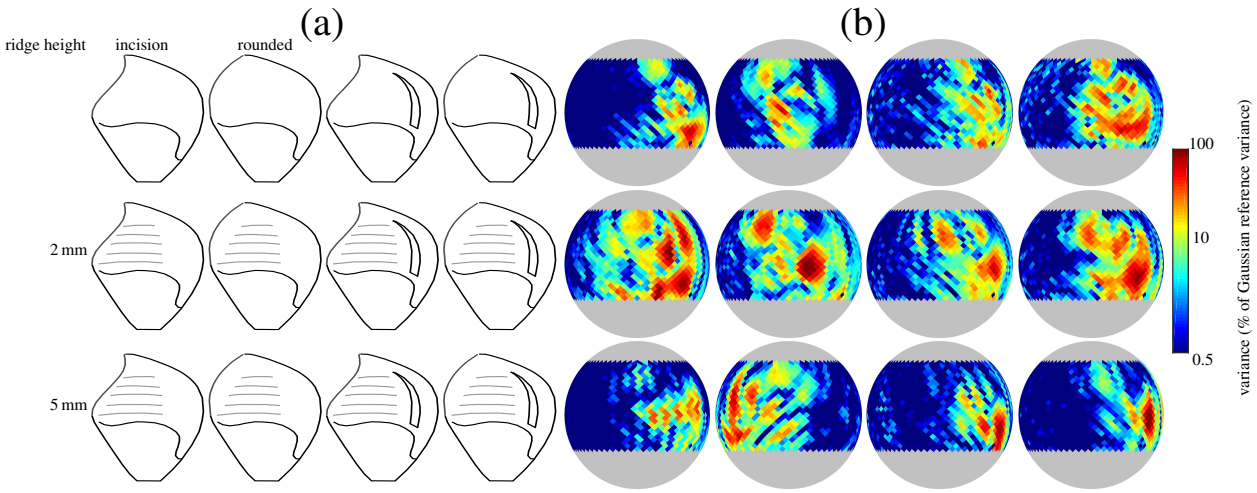

Figure 3.8: Reception signal variance across spatial direction for different ridge, incision and spine (always 5 mm) local shape feature combinations: each row and column entries correspond in (a) and (b)

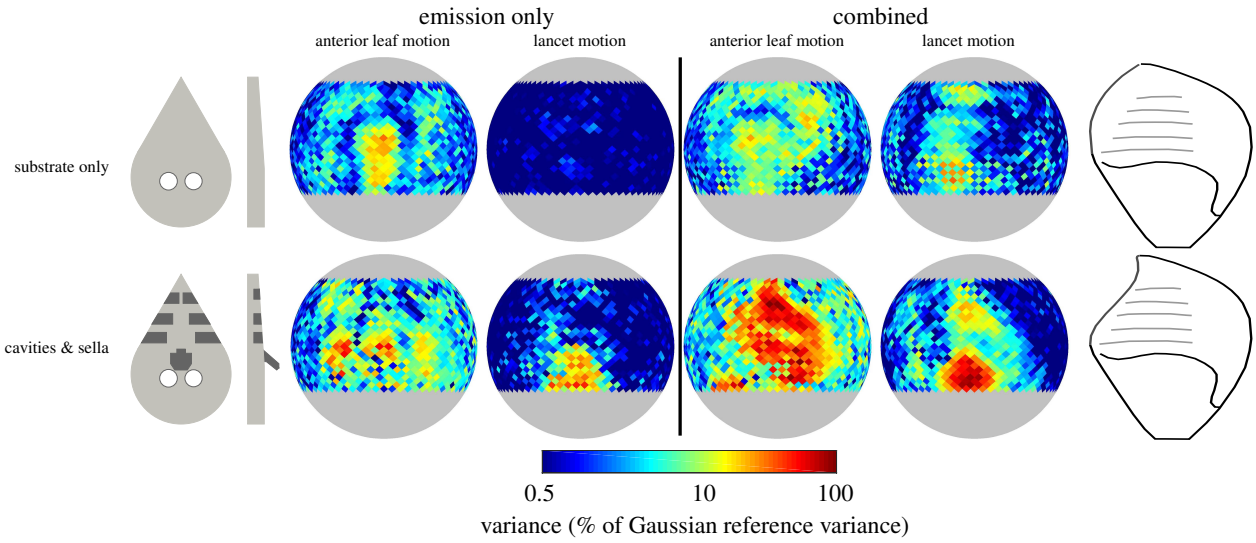

Figure 3.9: Emission and combined emitter and receiver signal variance across spatial direction for a noseleaf with two shape feature combinations and two independent motions, corresponding patterns pinnae for the combined patterns(2 mm ridges) shown on left: (i) symmetric anterior leaf motion and (ii) forward lancet flexion

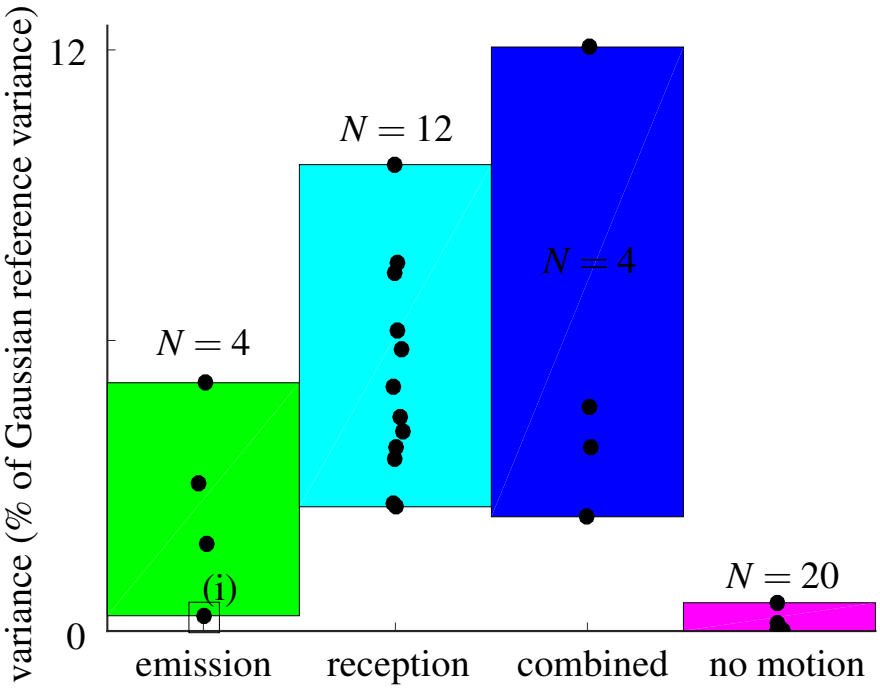

Figure 3.10: Average variance for dynamic emission, pinnae, combined, and no motion shape and motion categories: (i) noseleaf baffle without sella and lancet furrows, lancet motion only

3.5 Discussion

Results presented here demonstrate pinnae and noseleaf motions generate strong amplitude modulations across spatial direction and frequency. Pinnae without local shape features had less dynamics than baffles with features. However, pinnae with exaggerated feature combinations did not increase dynamics either. Instead, the pinnae with most dynamic properties had local shape features closest to the reference pinnae. Overall, the dynamic properties of the pinnae are generated by interactions between local shape features. This reflects previous

findings [41]. However what differs from previous findings is that there appears to be an optimum in pinnae feature geometry with respect the amount of dynamics generated since neither exaggerated local shape features nor featureless pinnae generated strong dynamics. Added furrows and sella features to the noseleaf generated more dynamics than the featureless noseleaf. However, more feature combinations in the noseleaf are necessary to elucidate the effect of local shape features.

Peak amplitude modulations in the pinnae and combinations of the noseleaf and pinnae had variances approaching a Gaussian variance bound. In general, the modulation variance generated by noseleaf motion was less than either the pinnae and combinations of the two. It should be noted the Gaussian bound used in this work was conservative since the spatial continuity of amplitude modulations was not conserved. Consequently, the spatial area approaching higher percentages of an upper bound might be even higher in both the noseleaf and pinnae if the bound accounted for spatial and time bandwidth.

The modulation patterns generated by the deforming pinnae appear fundamentally different from previously developed biomimetic sonar systems [66, 26]. The motions using flexible deforming pinnae and noseleaf changed the beampattern properties in azimuth and elevation. This is likely due to the difference between a flexible deforming receiver or noseleaf element and a rotating circular transducer [66, 26]. Further work is necessary to further elucidate the properties of the observed amplitude modulation patterns for actual sonar sensing tasks. To this authors knowledge, combining noseleaf motion with pinnae motion has not been attempted before. Combinations of the biomimetic dynamic emitter and receiver show that

for certain shape features under the motions studied in this work, increased dynamics can be generated beyond individual pinnae and noseleaf dynamics. However, further work remains since the motions studied here were carefully synchronized to coincide with incoming and outgoing sonar pulses. This is unlikely in real sensing operation since it assumes timing information *a priori*.

Chapter 4

Summary and Conclusions

4.1 Research accomplishments

Adaptations to the bat biosonar system were explored in two areas. In the first part, common beampattern features were found in a diverse set of beampatterns derived from different species noseleaf and pinnae shapes. In the second, the pinnae and noseleaf shape dynamics in horseshoe bats were mimicked using a biomimetic robot and the time-variant beampattern properties measured. In doing so, the following was accomplished:

- Developed a method to align 267 different beampatterns across 97 species to a common reference pattern using a pairwise global optimization approach.
- Decomposed the aligned beampatterns into eigenbeams using principal component analysis (PCA)

- Designed and built a comprehensive biomimetic model of shape and dynamics observed in the horseshoe bat's emission system
- Built a comprehensive biomimetic model of the horseshoe bats dynamic reception system
- Developed a bound on the observable dynamics using a white Gaussian noise model
- Evaluated a comprehensive set of local shape noseleaf and pinnae shape features' dynamic effects
- Measured for the first time the combination of emission and reception dynamics

4.2 Major Findings

- An optimal alignment between two beampatterns could be found by casting the alignment problem as an optimal rotation problem using a p-norm error metric. Furthermore, the search to find the optimal alignment could be limited to a region around the plane bisecting the gain weighted direction vector of each beampattern.
- The mean beampattern of 267 different species of bats consists of a simple symmetric lobe which narrows in beamwidth across frequency from 90° to 50°. Furthermore, the first three eigenbeams sharpen or broaden the mean beampattern lobe. However, non-trivial variance is captured by the eigenbeams above the first three. These higher

order eigenbeams were found to affect motion of the mean beampattern main lobe, generate sidelobes, and develop asymmetry in the lobes.

- Eigenbeams can capture taxonomic and functional differences in the beampatterns.
- For repeated motion patterns, systematic changes to pinnae or noseleaf local feature combinations resulted in strong *non-systematic* changes to the quality in which the beampattern lobes moved across spatial direction.
- Peak amplitude modulation variance across individual pinnae, noseleaf, and shape combinations thereof remained same within each category; however, the total spatial area covered by strong amplitude modulations differed by local shape feature combinations.
- Pinnae motions and combined noseleaf and pinnae motions for most local shape features generated greater amplitude modulations than noseleaf motions. However, the combinations of noseleaf and pinnae motions were highly sensitive to local shape feature combinations.

4.3 Discussion

Static and dynamic shape adaptations appear to change the bat's biosonar beampattern in similar ways. Along frequency, higher order eigenbeams add scanning motion to the mainlobe, asymmetry, and splitting of the main lobe into multiple sidelobes. Along time, motion of the pinnae and noseleaf redirect energy into sidelobes, generated asymmetry, and

add motion to the main lobe. Hence, these two shape adaptations appear to do similar things to the beampattern but through different mechanisms. Eigenbeams suggest there is strong variance in beampattern properties across frequency. Thus, changing the frequency of the sonar call generates different spatial qualities to the emitted and received beampattern. Similarly, motion of the pinnae and noseleaf baffles generated same types of changes to the beampatterns in time. However, shape adaptations have less extensibility to adapting to new environmental scenarios than motion since bats that feature pinnae and noseleaf motion have adaptive mechanisms they can use during biosonar operation while static shape features remain the same. Indeed, horseshoe bats appear to exhibit more pinnae dynamics when confronted with new environments [48].

In either case, static shape adaptations and motion represent radical departures from today's technology. Given the state of the art currently lags bat biosonar, bats offer a strong model for bioinspiration. In particular, this work has shown that two things matter in bat biosonar beampatterns: shape and motion. As techniques for constructing bioinspired sonars, shape and motion offer two mechanisms to achieve the same goal: diversity across spatial direction in the beampattern transfer function properties.

4.4 Suggestions for future work

- Beampattern variance was decomposed in this work. However, a beampattern is a function of shape and principle component analysis would readily extend to joint de-

composition of shape and beampattern variance. This type of analysis might yield insight neither decomposition of the beampattern or shape variance could.

- Using the dynamic sonar substrate developed in this work to perform sonar tasks like localization, classification, and navigation

Bibliography

[1] J. D. Altringham. *Bats: from evolution to conservation*. Oxford University Press, New York, 2011.

[2] H. Arita. Noseleaf morphology and ecological correlates in phyllostomid bats. *J Mammal*, 71(1):36–47, 1990.

[3] M. Aytekin, E. Grassi, M. Sahota, and C. F. Moss. The bat head-related transfer function reveals binaural cues for sound localization in azimuth and elevation. *J. Acoust. Soc. Am.*, 116(6):3594, 2004.

[4] A. Ben-Hur and J. Weston. A users guide to support vector machines. In Oliviero Carugo and Frank Eisenhaber, editors, *Data Mining Techniques for the Life Sciences*, volume 609, pages 223–239. Humana Press, 2010.

[5] J. Blauert. *Spatial hearing: the psychophysics of human sound localization*. MIT Press, 1997.

[6] J. Y. Bouguet. Camera calibration toolbox for matlab. 2004.

[7] P. Caspers, A. Leonessa, and R. Müller. Eigenbeam analysis of the diversity in bat biosonar beampatterns. *J. Acoustic Soc.*, 135(4):2207–2207, 2014.

[8] P. Caspers, R. Pan, A. Leonessa, and R. Müller. The alignment problem for bat biosonar beampatterns. *Proceedings of Meetings on Acoustics*, 19(1), 2013.

[9] G. S. Chirikjian and A. B. Kyatkin. *Engineering applications of noncommutative harmonic analysis*. CRC Press, Boca Raton, FL, 2000.

[10] L. Feng, G. Li, H. Lu, and R. Müller. Noseleaf dynamcis during pulse emission in horseshoe bats. *PLOS One*, 7(5):e34685, May 2012.

[11] Neville H. Fletcher. *Acoustic Systems in Biology*. Oxford University Press, 1992.

[12] N.H. Fletcher and S. Thwaites. Obliquely truncated simple horns: Idealized models for vertebrate pinnae. *Acustica*, 65:194–204, 1988.

[13] L. Gao, S. Balakrishnan, W. He, Z. Yan, and R. Mller. Ear deformations give bats a physical mechanism for fast adaptation of ultrasonic beam patterns. *Phys. Rev. Lett.*, 107(21):214301, Nov. 2011.

[14] J. Gaudette. *Bio-Inspired broadband sonar: methods for acoustical analysis of bat echolocation and computation modeling of biosonar signal processing*. PhD thesis, Brown University, 2014.

[15] K. M. Gorski, E. Hivon, A. J. Banday, B. D. Wandelt, F. K. Hansen, M. Reinecke, and M. Bartelman. HEALPix – a framework for high resolution discretization, and fast analysis of data distributed on the sphere. *Astrophys. J.*, 622(2):759–771, 2050.

[16] D. R. Griffin and D. C. Dunning. Correlated orientation sounds and ear movements of horseshoe bats. *Nature*, 4860:1185–1188, 1962.

[17] R. Griffin. *Listening in the dark, the acoustic orientation of bats and men.* Dover, 1974.

[18] A. Gupta, D. Webster, and R. Müller. Interplay of lancet furrows and shape change in the horseshoe bat noseleaf. *The Journal of the Acoustical Society of America*, 138(5):3188–3194, 2015.

[19] W. He, S. Pedersen, A. Gupta, J. Simmons, and R. Müller. Lancet dynamics in greater horseshoe bats, *Rhinolophus ferrumequinum*. *PLoS One*, 10(4):1–13, Apr. 2015.

[20] J. Heikkila and O. Silvén. A four-step camera calibration procedure with implicit image correction. In *Computer Vision and Pattern Recognition, 1997. Proceedings., 1997 IEEE Computer Society Conference on*, pages 1106–1112. IEEE, 1997.

[21] R. A. Horn and C. R. Johnson. *Matrix Analysis.* Cambridge University Press, New York, 2nd edition, 2012.

[22] JF. Hughes. *Computer graphics: principles and practice.* Addison-Wesley, Upper Saddle River, New Jersey, 3rd. edition, 2014.

[23] I. T. Jolliffe. *Principal Component Analysis.* Springer-Verlag, New York, 2002.

[24] G. Jones and E. Teeling. The evolution of echolocation in bats. *Tren. Ecol. Evol.*, 21(3):149–156, 2006.

[25] P. Kounitsky, J. Rydell, E. Amichai, A. Boonman, O. Eitan, A. Weiss, and Y. Yovel. Bats adjust their mouth gape to zoom their biosonar field of view. *Proc. Natl. Acad. Sci. U.S.A.*, 112(21):6724–6729, 2015.

[26] R. Kuc. Biologically motivated adaptive sonar system. *J. Acoust. Soc. Am.*, 100(3):1849–1854, Sep. 1996.

[27] B. D. Lawrence and J. A. Simmons. Echolocation in bats: the external ear and perception of vertical positions of targets. *Science*, 218(4571):481–483, Oct. 1982.

[28] L. Lazure and B. Fenton. High duty cycle echolocation and prey detection by bats. *J Exp Biol*, 214(7):1131–1137, 2011.

[29] Stanley G Lemon. Towed-array history, 1917-2003. *IEEE Journal of Oceanic Engineering*, 29(2):365–373, 2004.

[30] J. Ma and R. Müller. A method for characterizing the biodiversity in bat pinnae as a basis for engineering analysis. *Bioinspir. Biomim.*, 6(2):026008, 2011.

[31] MATLAB. *version 8.1.0.604 (R2013a)*. The MathWorks Inc., Natick, Massachusetts, 2013.

[32] N. Matsuta, S. Hiryu, E. Fujioka, Y. Yasufumi, H. Riquimaroux, and Y. Watanabe. Adaptive beam-width control of echolocation sounds by cf-fm bats, *Rhinolophus ferrumequinum nippon*, during prey-capture flight. *J. Exp. Biol.*, 216:1210–1218, 2013.

[33] maxon motor ag. *EPOS2 P Programmabel Positioning Controllers: Supervisory Control Reference*, May 2016.

[34] S. Meymand, M. Pannala, and R. Müller. Characterization of the time-variant behavior of a biomimetic beamforming baffle. *J. Acoust. Soc. Am.*, 133(2):1141–1150, 2013.

[35] J. Mogdans, J. Ostwald, and H. Schnitzler. The role of pinna movement for the localization of vertical and horizontal wire obstacles in the greater horseshoe bat, *Rhinolopus ferrumequinum*. *J. Acoust. Soc. Am.*, 84(5):1676–1679, 1988.

[36] M. Motamedi, X. Quiping, and R. Müller. Characterization of the diversity in bat biosonar beampatterns with spherical harmonics power spectra. *J. Acoust. Soc. Am.*, 132:1895, 2012.

[37] R. Müller. Numerical analysis of biosonar beamforming mechanisms and strategies in bats. *J. Acoust. Soc. Am.*, 128(3):1414, 2010.

[38] R. Müller and R. Kuc. Biosonar-inspired technology: goals, challenges and insights. *Bioinspiration & Biomimetics*, 2(4):S146, 2007.

[39] R. Müller, H. Lu, and J. R. Buck. Sound-diffracting flap in the ear of a bat generates spatial information. *Phys. Rev. Letters*, 100(10):108701, 2008.

[40] R. Müller, A. Mubeezi-Magoola, H. Peremans, J. Hallam, S. Jones, J. Flint, D. Reynaerts, H. Bruyninckx, R. Lerch, and A. Streicher. Chiroptera-inspired robotic cephaloid (circe): A next generation biomimetic sonar head. *J. Acoust. Soc. Am.*, 112(5):2335–2335, 2002.

[41] R. Müller, M. Pannala, O. P. Reddy, and S. Meymand. Design of a dynamic sensor inspired by bat ears. *Smart Mater. Struct.*, 21(9):094025, Aug. 2012.

[42] G. Neuweiler. Auditory adaptations for prey capture in echolocating bats. *Physiol. Rev.*, 70(3):615–637, July 1990.

[43] M. K. Obrist, M. B. Fenton, J. L. Eger, and P. A. Schlegel. What ears do for bats: a comparative study of pinna sound pressure transformation in chiroptera. *J. Exp. Biol.*, 180(1):119–152, 1993.

[44] R. Pan, V. Skala, and R. Müller. Globally optimal rotation alignment of spherical surfaces with associated scalar values. *3D Research*, 4(3), 2013.

[45] S.. Pedersen and R. Müller. *Nasal-Emission and Nose leaves*, pages 71–91. Springer New York, New York, NY, 2013.

[46] H. Peremans and R. Müller. A comprehensive robotic model for neural & acoustic signal processing in bats. In *Neural Engineering, 2003. Conference Proceedings. First International IEEE EMBS Conference on*, pages 458–461. IEEE, 2003.

[47] J. Pye and L. Roberts. Ear movements in a hipposiderid bat. *Nature*, 225:285–286, 1970.

[48] J.D. Pye, M. Flinn, and A. Pye. Correlated orientation sounds and ear movements of horseshoe bats. *Nature*, 196:1186–1188, 1962.

[49] J. Ratcliffe, C. Elemans, L. Jakobsen, and A. Surlykke. How the bat got its buzz. *Biol. Lett.*, 9(2), 2013.

[50] D. M. Renwick. Marine mammals are a force multiplier. *Proceedings Magazine*, 123(8):134, Aug. 1997.

[51] H. Schneider and FP Möhres. Die ohrbewegungen der hufeisennasenfledermäuse (chiroptera, rhinolophidae) und der mechanismus des bildhörens. *Z Vergl Physiol.*, 44(1):1–40, Jan. 1960.

[52] H. Schnitzler and A. Grinnell. Directional sensitivity of echolocation in the horseshoe bat, *Rhinolophus ferrumequinum*. *J. Comp. Physiol.*, 116(1):51–61, Nov. 1977.

[53] Hans-Ulrich Schnitzler and Elisabeth K. Kalko. Echolocation by insect-eating bats. *BioScience*, 51(7):557–569, 2001.

[54] H.U. Schnitzler and E. Kalko. Echolocation by insect-eating bats. *BioScience*, 51(7):557–569, 2001.

[55] H.U Schnitzler, E. Kalko, I. Kaipf, and A. Grinnell. Fishing and echolocation behavior of the greater bulldog bat, *Noctilio leporinus*, in the field. *Behav Ecol Sociobiol*, 35(5):327–345, 1994.

[56] H.U. Schnitzler, C. F. Moss, and A. Denzinger. From spatial orientation to food acquisition in echolocating bats. *Trends Ecol Evol*, 18(8):386–394, 2003.

[57] M. D. Schuster. A survey of attitude representations. *Journal of Astronautical Sciences*, 1993.

[58] M. Skolnik. *Introduction to Radar Systems*. McGraw-Hill, 2001.

[59] J. Streelman and P. D. Danley. The stages of vertebrate evolutionary radiation. *Trends Ecol Evol*, 18(3):126131, 2003.

[60] A. Surlykke, L. Miller, B. Møhl, B. Andersen, J. Christensen-Dalsgaard, and M. Jørgensen. Echolocation in two very small bats from thailand: *Craseonycteris thonglongyai* and *Myotis siligorensis*. *Behav Ecol Sociobiol*, 33(1):1–12, 1993.

[61] M. Turk and A. Pentland. Eigenfaces for recognition. *J. Cognitive Neuroscience*, 3(1):71–86, 1991.

[62] Robert J. Urick. *Principles of underwater sound*. McGraw-Hill, New York, 3rd edition, 1983.

[63] D. Vanderelst, F. De Mey, H. Peremans, I. Geipel, E. Kalko, and U. Firzlaff. What noseleaves do for fm bats depends on their degree of sensorial specialization. *PLoS ONE*, 5(8):1–13, Aug. 2010.

[64] D. Vanderelst, J. Reijnier, J. Steckel, and H. Peremans. Information generated by moving pinnae of *Rhinolophus rouxii*: tuning of the morphology at different harmonics. *PLos One*, 6(6):e20627, 2011.

[65] J. Vince. *Quaternions for Computer Graphics*. Springer London, 2011.

[66] V. A. Walker, H. Peremans, and J. C. T. Hallam. One tone, two ears, three dimensions: A robotic investigation of pinnae movements used by rhinolophid and hipposiderid bats. *J. Acoust. Soc. Am.*, 104(1):569–579, 1998.

[67] D. Wilson and D. Reeder. *Mammal species of the world: A taxonomic and geographic reference*, volume 1. Johns Hopkins University Press, Baltimore, MD, 2005.

[68] W. Wirth. *Radar Techniques Using Array Antennas (2nd Edition)*. The Institution of Engineering and Technology, London, U.K., 2013.

[69] J. M. Wotton, T. Haresign, and J. A. Simmons. Spatially dependent acoustic cues generated by the external ear of the big brown bat, eptesicus fuscus. *J. Acoust. Soc. Am.*, 98(3):1423–1445, 1995.

[70] F. Yanqing, P. Caspers, and R. Müller. A dynamic ultrasonic emitter inspired by horseshoe bat noseleaves. *Bioinspir. Biomim.*, 11(3):036007, 2016.

[71] A. Yershova, S. Jain, S. M. LaValle, and J. C. Mitchell. Generating uniform incremental grids on SO(3) using the hopf fibration. *Int. J. Robot. Res.*, 29(7):801–812, 2010.

[72] X. Yin, P. Nguyen, T. J. Tucker, and R. Müller. A comparative study of pinna motions in horseshoe bats and old world leaf-nosed bats. *J. Acoust. Soc. Am.*, 138(3):1761–1761, 2015.

[73] Q. Zhuang and R. Müller. Numerical study of the effect of the noseleaf on biosonar beamforming in a horseshoe bat. *Phys. Rev. E.*, 76(5):051902, 2007.

[74] Q. Zhuang, X. Wang, M. Li, J. Mao, and F. Wang. Noseleaf pit in egyptian slit-faced bat as a doubly curved reflector. *EPL*, 97(4):44001, 2012.